DOI https://doi.org/10.32782/1994-4691-2026-1-77-7
УДК 510.621.9

COMPONENTS OF HYDRAULIC CONTROL SYSTEMS FOR WHEELLESS GROUND ROBOTIC COMPLEXES

ЕЛЕМЕНТНА БАЗА СИСТЕМ ГІДРОАВТОМАТИКИ БЕЗКОЛІСНИХ НАЗЕМНИХ РОБОТИЗОВАНИХ КОМПЛЕКСІВ

V. Strutynsky[1*], Dr. Tech. Sciences, Professor ORCID: 0000-0001-7167-0085

[1] *National Technical University of Ukraine "Igor Sikorsky Kyiv Polytechnic Institute", Kyiv, Ukraine*
* e-mail: vbstrutynskiy@gmail.com

Abstract. The article addresses the development of components for hydraulic control systems of wheelless ground robotic complexes with high terrain mobility. Typical wheelless ground robotic complexes are considered. They have a central section that slides along the surface using inertial propulsion devices and is equipped with long, flexible peripheral elements, 2–3 m in length, with knives, saws, or milling cutters mounted at their ends to break down obstacles. The complex has a large manipulator, approximately 4 m in length, which provides surface inspection and examination, orientation, and communication. Wheelless ground robotic complexes include special units, hydraulic drives, and hydraulic control systems using industrial water as the working fluid. It is proposed to implement them using innovative components based on high-pressure jet and vortex devices and units operating at approximately 25 MPa. The developed schematic solutions for innovative jet and vortex devices are presented. The hydrodynamic processes in the devices were investigated theoretically and experimentally. It was established that singular flow regions, where the rate-of-strain tensor becomes degenerate, determine the operating processes of jet and vortex devices. The results of studies of the static and dynamic characteristics of the jet devices forming the set of components are presented. A structural design and manufacturing methods are proposed for small channels, approximately 0.3 mm in size, with increased wear resistance. The manufacturing methods were tested using experimental prototypes that were designed and manufactured.

Keywords: jet units, vortex devices, singular regions, turbulent jets, static characteristics.

Introduction.

Special-purpose ground robotic complexes are widely used in humanitarian demining [1]. Therefore, research aimed at developing advanced designs of ground robotic complexes is relevant. The proposed special-purpose ground robotic complexes have a central section that moves along the surface using inertial propulsion devices. This section is equipped with long, flexible peripheral elements, 2–3 m in length, with knives, saws, or milling cutters mounted at their ends to break down obstacles.

Ground robotic complexes operate under off-road conditions [2], with considerable variations in temperature and humidity and without the necessary repair facilities and equipment. Therefore, the general problem is to improve the reliability of these complexes under harsh operating conditions [3]. One aspect of this problem is to improve their terrain mobility [4]. This is consistent with practical applications of ground robotic complexes [5] and general trends in the development of mobile robots [6].

Literature Review.

A reasonable approach to improving terrain mobility is to develop wheelless robots that move by sliding [7]. Several technical solutions for wheelless ground robotic complexes have been developed [8]. An analysis of the literature [9] indicates that snake-like robotic

complexes are a promising direction.

The use of mechatronic systems is recommended to improve robot performance [10]. The performance of mechatronic systems [11, 12] largely depends on their dynamic characteristics [13]. The use of hydraulic and pneumatic control systems and hydraulic drives is promising [14, 15]. These systems help address the challenges of operating wheelless robots under difficult temperature and humidity conditions [16].

The use of mineral oil as the working fluid in the hydraulic drives of ground robotic complexes is not considered appropriate [17]. Industrial water is a reasonable alternative. However, its use creates several problems in the development of hydraulic and pneumatic control systems for ground robotic complexes [18]. The main problem is the inability to achieve the required fineness of working fluid filtration [19].

An analysis of the literature discussed above and other information sources [1, 6] indicates that clear proposals for the development of wheelless ground robotic complexes are currently lacking. Recommendations for the use of control components are also unavailable. Therefore, the development of components for hydraulic and pneumatic control systems remains an unresolved aspect of the broader problem of developing advanced ground robotic complexes.

The aim of this study is to develop fundamentally new components for hydraulic and pneumatic control systems based on high-pressure jet and vortex devices that use industrial water containing a considerable amount of contaminants as the working fluid. The proposed high-pressure jet devices are adapted for use in wheelless ground robotic complexes.

Research Methodology.

To achieve this aim, the following research objectives were formulated and addressed:

- to analyse the specific operating conditions of hydraulic control systems in wheelless ground robotic complexes;
- to develop schematic and design solutions for high-pressure jet and vortex devices;
- to investigate the operating processes in jet and vortex devices;
- to determine the specific features of the characteristics of the devices forming the set of control components;
- to identify promising design and manufacturing approaches for developing components of hydraulic and pneumatic control systems for wheelless ground robotic complexes.

The study used materials from a wide range of engineering developments, including innovative designs, results from tests of experimental prototypes of jet and vortex devices, and operating experience with jet and vortex devices, including series-produced devices, in various engineering applications [20, 21]. These materials were adapted to the development of components for hydraulic control systems in wheelless ground robotic complexes [2, 22].

Theoretical and experimental methods were used in the study. The hydrodynamic processes in jet and vortex devices were investigated by numerical integration of the governing equations of fluid mechanics. The finite element and finite difference methods were applied.

The theoretical calculations of jet and vortex flows were confirmed by experimental data obtained through flow visualisation in model jet devices. In these experiments, MS-20 oil containing a finely dispersed gas phase flowed at velocities of up to 50 m/s. High-pressure turbulent flows at 20–30 MPa were investigated using miniature Pitot tubes, 0.2–0.3 mm in size, on a specially designed test rig that provided positioning accuracy of 0.5–1 μm for the device components. The equipment and measuring instruments used provided a measurement accuracy of 1–2%.

Special methods were developed and used to investigate high-pressure fluid flows in jet devices. An effective method involves analysing singular regions in the moving fluid where the stress tensor and the rate-of-strain tensor become degenerate. Innovative methods for investigating the operating processes were proposed based on an analysis of wear in jet device

parts after 10 million operating cycles.

Both analytical and experimental methods were used to investigate the static characteristics of the devices forming the set of control components. The theoretical analysis of the characteristics of jet and vortex devices was based on solving the equations of fluid mechanics in integral form [20]. Experimental studies were conducted using specially designed test equipment. This equipment made it possible to measure the static characteristics of jet devices with assembled nozzles and receiver channels measuring 0.1–1 mm, at operating pressures of up to 30 MPa and flow rates of up to 15 l/min.

The theoretical study of the dynamic characteristics of jet devices was based on fuzzy and stochastic mathematical models [16, 23]. The computational models accounted for the inertia and compressibility of the working fluid. Experimental studies of the dynamic behaviour were conducted using high-precision pressure sensors. The measurement results were processed using statistical methods and specialised software to determine correlation functions, spectral densities, and other characteristics of dynamic processes in jet devices.

Advanced manufacturing and metalworking methods were used to produce the main control components [24, 25]. On this basis, innovative designs were developed for assemblies and parts of jet and vortex devices forming the components of hydraulic control systems in wheelless ground robotic complexes. Manufacturing issues related to the main parts of jet and vortex devices were addressed.

Results.

Developed Ground Robotic Complexes

Several schematic and design solutions for wheelless ground robotic complexes have been developed. The most effective are ground robotic complexes that incorporate flexible elements. The developed wheelless ground robotic complex has a central section 1 containing batteries as the power source, a hydraulic power unit, and a control system (Fig. 1).

The front section 2 of the ground robotic complex is connected to the central section. It carries a rotating milling cutter 3 with its drive. The rear section of the wheelless robot consists of two branches, 4 and 5, attached to the central section 1. The ends of the rear branches are equipped with positioning devices in the form of rotors 6 and 7, which have ribs for interaction with the ground. The rotors are powered by drives located in the end modules 8 and 9 of the rear branches. The front section 2 and the rear branches 4 and 5 consist of flexible modules connected in series. These modules allow limited spatial movement of the front and rear sections relative to the central section 1.

The front section 2 moves in the horizontal plane so that the milling cutter sweeps an arc $F_1F_0F_2$ whose width B_n exceeds the overall width B_a of the rear section of the robot. As a result, the milling cutter breaks down obstacles in the robot's path, allowing the robot to move freely along the x-axis.

The front section of the ground robotic complex can move vertically. During this movement, the milling cutter follows an arc $F_3F_0F_4$ (see Fig. 1b). Its vertical sweep H_n exceeds the overall height H_a of the robot with the manipulator mounted on it. Obstacles in the robot's path are therefore broken down to provide sufficient clearance for the robot and its manipulator to pass.

The large manipulator, with a total length of approximately 4 m, has a main link 10 of length L_1. Links 11 and 12 form the main linkage of the manipulator. The links are connected by single-axis joints A_0 and B_0. The manipulator has a static balancing system consisting of a balancing lever 13 connected to link 10 and a balancing mass 14. A hexapod mechanism 15 is mounted at the end of link 12 for fine spatial movements of the tactile device 16.

In the folded position, the manipulator is placed and secured on the rear section of the robot, while the balancing lever 13 is secured on the front section. Link 10 is mounted on the rotary base 17 through a two-axis joint O. Link 11 has an aerodynamic control system consisting of a propeller 18 and its drive.

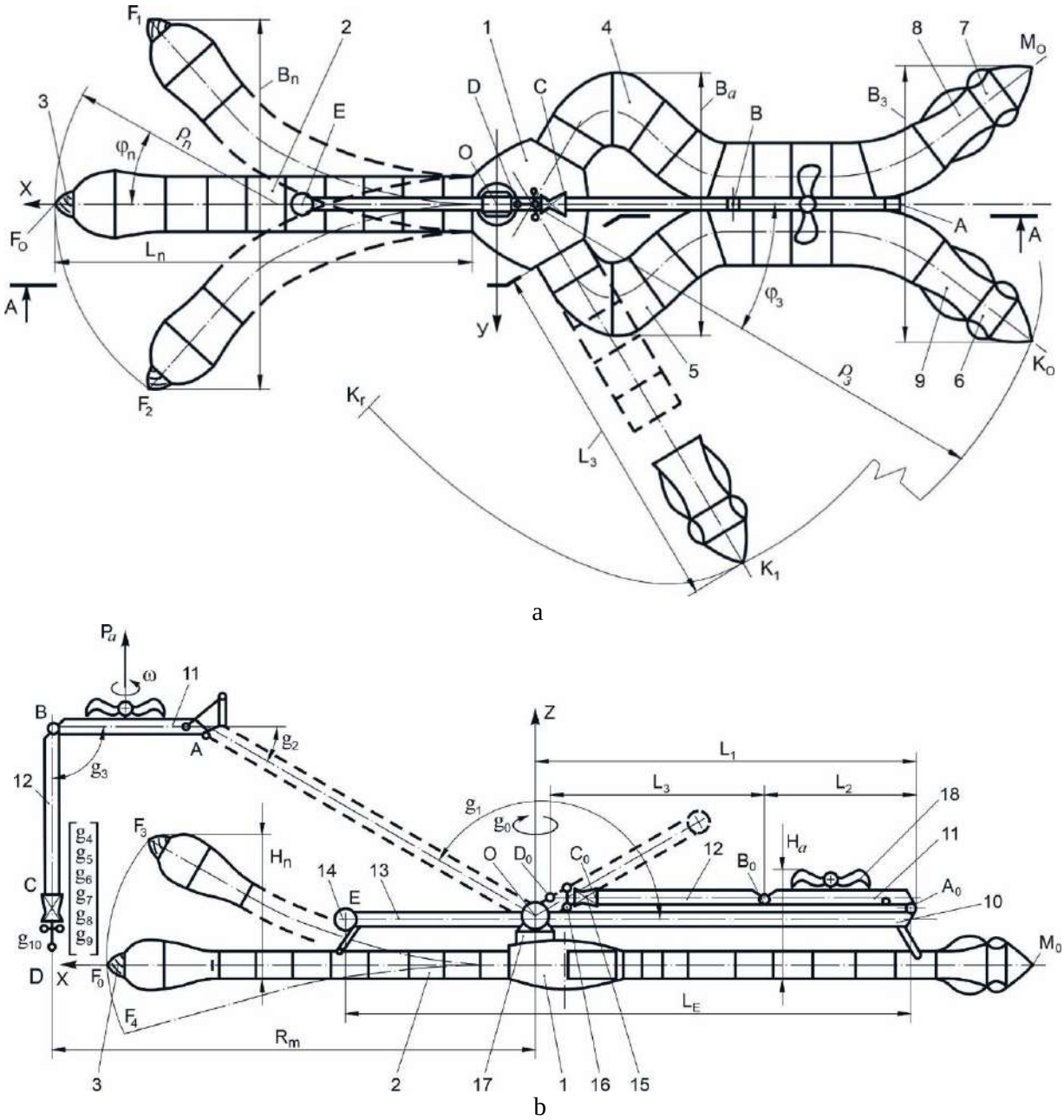


Fig. 1. Typical wheelless ground robotic complex: (a) top view; (b) side view; 1 – central section; 2 – front section; 3 – rotating milling cutter; 4, 5 – rear branches; 6, 7 – working rotors; 8, 9 – end modules; 10 – main link; 11, 12 – links; 13 – balancing lever; 14 – balancing mass; 15 – hexapod mechanism; 16 – tactile device; 17 – rotary base; 18 – propeller.

In the operating position, the manipulator assumes the configuration *OABCD*. Link 11 is positioned so that its axis (*AB*) is nearly horizontal. The propeller lift vector P_a is directed approximately along the direction of the gravitational forces acting on the manipulator. Changing the direction of the propeller lift vector allows the position of the tactile device to be adjusted within the region *D*. The manipulator has the required number of controlled coordinates.

The drives for coarse (rapid, macro-scale) movements provide rotation of the manipulator (coordinate q_0), adjustment of the position of link 10 through an angle q_1, adjustment of the relative angular position of links 10 and 11 through an angle q_2, and variation of the angle q_3 between links 11 and 12. To improve positioning accuracy, the manipulator is equipped with a six-coordinate fine-positioning drive implemented as a hexapod mechanism 15 with six degrees of freedom: q_4, q_5, …, q_9 [26].

Three controlled coordinates of the hexapod provide translational movements of the tactile device 16, while the other three provide its angular movements in space. The tactile device has an additional controlled coordinate q_{10}, which determines the position of point D relative to the hexapod platform.

Thus, in its operating position, the manipulator has 10 controlled coordinates. Its workspace is bounded by a spherical surface with a radius $R=max(R_m)=L_1+L_2+L_3$. To ensure reliable operation of the manipulator without loss of static equilibrium, the wheelless robot must have a sufficient support area. When the manipulator is positioned close to the plane *xoz*, the front section 2 and the rear branches 4 and 5, extending along the axis *x*, provide this support area. The outermost points F_0, K_0 and M_0 define the limits of the support areas.

The flexibility of the front and rear sections should be taken into account when determining the static stability of the manipulator. Positioning the manipulator away from the robot's plane of symmetry requires support areas located away from the plane *xoz*. The maximum distance of the front section (points F_1 and F_2) from the axis *x* is determined by the possible deformation of the elastic front section 2.

The width B_n of the arc can be used to estimate the extent of the support area provided by the front section. The support areas at the rear of the robot are formed at points K_0 and M_0. If necessary, the rear branches 4 and 5 change their configuration to increase the distance between their outermost points. A straight configuration of the branches is a reasonable choice and corresponds to the movement of point K_0 along the curve $K_0K_1K_2$. The region in which branch 5 can be positioned is bounded by the curve whose radius ρ_3 depends on the angle φ_3.

Changing the position of the rear branches significantly affects the robot's terrain mobility. Moving branches 4 and 5 and their end modules 8 and 9 away from the axis *x* allows the robot to generate resistance forces to withstand the cutting forces of the milling cutter. Wave-like movements of the rear branches provide translational motion of the robot in different directions. The ability to turn in the plane *xoy* is particularly important. This compensates for a limitation of a robot with a linear configuration, for which turning is a difficult operation.

The presence of three long, flexible elements reduces the likelihood of unwanted twisting of the flexible branches, which is characteristic of robots with a linear configuration. The robot can also move backwards along the axis *x*. The proposed design improves the reliability of robot operation when travelling over rough terrain with steep slopes.

Features of Hydraulic and Pneumatic Control Systems of Ground Robotic Complexes

According to the basic design scheme [27], the front section 2 of the wheelless robot has a rotating milling cutter 1 mounted on a spherical fluid-film bearing with a sphere 3 (Fig. 2).

The milling cutter 1 is rotated by a high-torque hydraulic motor 17 controlled by a directional control valve 18. The hydraulic motor shaft is connected to the sphere 3 through an involute gear coupling 19. The geometric centre of the coupling 19 is located at the centre of the sphere 3. This allows limited spatial rotation of the sphere 3. The sphere can rotate through an angle φ_0 in the *xoy* plane and through an angle θ_0 in the perpendicular *xoz* plane.

The sphere is rotated in these planes by hydraulic drives. They include hydraulic cylinders 20 and 21 controlled by a directional control valve 22. The piston rods interact with the outer part of a rolling-element bearing 23 mounted on a shank 24 attached to the sphere 3. Hydraulic cylinders 20 and 21 rotate the sphere 3 through an angle φ_0 in the *xoy* plane. Similar drives with a corresponding directional control valve are used to rotate the sphere in the perpendicular *xoz* plane (not shown in the figure).

The spherical fluid-film bearing has a series of hydrostatic bearings 25 supplied with fluid through throttles 26 from the robot's common high-pressure line 27. Fluid is drained from the spherical fluid-film bearing through a drain line 28 connected to its low-pressure cavity 29. The spherical fluid-film bearing also has a series of hydrodynamic bearings 30.

Various cutting forces act on the milling cutter 1.

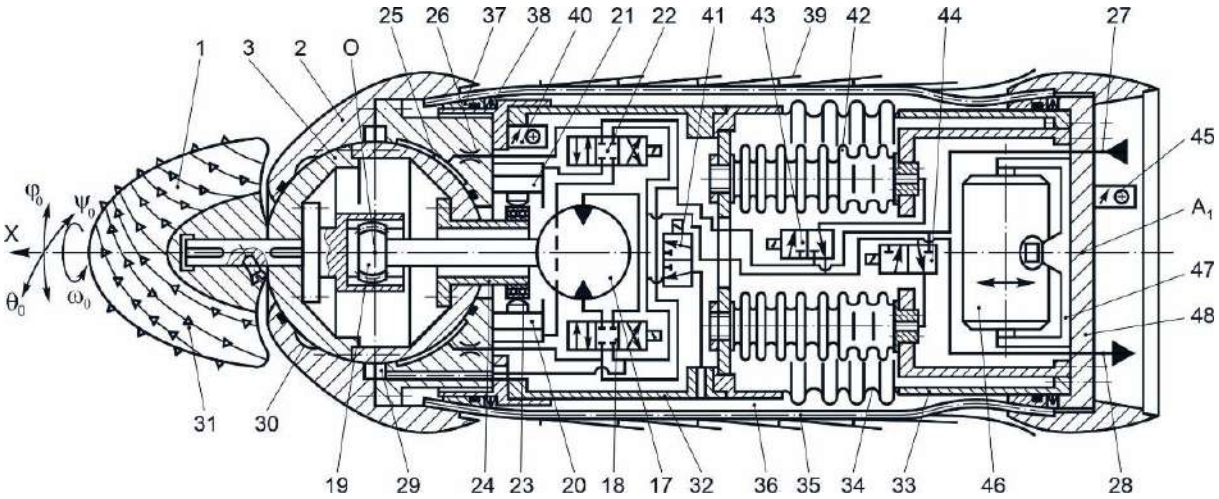


Fig. 2. Design scheme of the front section of the wheelless robot: 1 – milling cutter; 2 – front section of the robot; 3 – sphere; 17 – high-torque hydraulic motor; 18 – directional control valve; 19 – involute gear coupling; 20, 21 – hydraulic cylinders; 22 – directional control valve; 23 – rolling-element bearing; 24 – shank; 25 – hydrostatic bearings; 26 – throttles; 27 – common high-pressure line of the robot; 28 – drain line; 29 – low-pressure cavity of the spherical bearing; 30 – hydrodynamic bearings; 31 – inserts made of superhard materials; 32, 33 – tubular elements; 34 – bellows; 35 – outer elastic shell; 36 – sealed annular cavity; 37 – movable conical sleeves; 38 – disc springs; 39 – protective plates; 40 – gyroscopic inertial navigation device for tubular element 32; 41 – directional control valve for regulating the pressure in the annular cavity; 42 – bellows-type actuators; 43, 44 – directional control valves for controlling the bellows-type actuators; 45 – gyroscopic inertial navigation device for tubular element 33; 46 – vibration device; 47 – fixed base of the vibration device; 48 – plate.

The maximum forces act in the direction opposite to the x-axis. They are supported by the system of hydrostatic bearings 25. The milling cutter 1 is made of a high-hardness material. To improve the efficiency of the cutting process, inserts 31 made of superhard materials are placed on the cutter surface. The use of synthetic diamonds, boron nitride, or boron carbide for these inserts is promising. The systematically arranged inserts ensure effective destruction of obstacles such as metal structures, barbed wire, concrete, stone, and other materials.

The efficiency of the cutting process is ensured by the proposed technical solution, which provides spatial rotations of the sphere 3 about the *x*, *y*, and *z* axes. The rotating milling cutter 1, connected to the sphere 3, acts as a gyroscope rotating at a frequency ω_0. Hydraulic cylinders 20 and 21, together with the hydraulic cylinders located in the plane perpendicular to the plane of the figure, do not rigidly fix the shank 24 mounted on the sphere 3. The cutting forces produce considerable spatial torques acting on the rotating milling cutter. These torques give rise to corresponding gyroscopic moments and cause precessional motion of the sphere and the milling cutter.

Spatial movement of the sphere allows useful force effects to be generated. For example, a sudden movement of the shank 24 in the xoy plane produces a considerable gyroscopic moment acting on the wheelless robot in the *xoz* plane. This can raise the front section of the robot above the ground surface or push it into the soil.

The front section of the robot contains tubular elements 32 and 33 connected by a bellows 34. These elements and the bellows are enclosed by an outer elastic shell 35, forming a sealed annular cavity 36. The edges of the elastic shell are sealed by movable conical sleeves 37. The sleeves are moved by disc springs 38. This ensures sealing and secures the elastic shell relative to tubular elements 32 and 33. Protective plates 39 are attached to the

shell surface. A special gyroscopic inertial navigation device 40 is used to measure the spatial position of tubular element 32.

The pressure in the annular cavity 36 is regulated by a directional control valve 41. The shell 35 is reinforced with cords made of ultra-high-strength fibre, oriented along the axes of tubular elements 32 and 33. As the pressure in cavity 36 increases, the elastic shell 35 expands in the diametrical direction. The reinforcing cords shorten the shell, compressing the bellows 34 and displacing tubular elements 32 and 33. Actuators for their relative spatial displacement are installed inside the tubular elements. A reasonable solution is to use bellows-type actuators 42 controlled by directional control valves 43 and 44. It is advisable to use three or more bellows-type actuators to provide relative spatial displacement of tubular elements 32 and 33.

A special gyroscopic inertial navigation device 45 is used to measure the spatial position of tubular element 33. A vibration device 46 is installed inside tubular element 33. It allows the direction of movement of its inertial mass to be adjusted. This device produces movement of the mass and, consequently, inertial loads in the *xoz* plane. The vibration device has a fixed base 47 attached to a plate 48 connected to tubular element 33.

The drive mechanisms of all parts of the ground robotic complex include an extensive hydraulic control system. Its main components, the first- and second-stage amplifiers, form the basis of the system's set of control components.

A specific feature of the hydraulic control system is the compact arrangement of devices within enclosed spaces. This requires minimising the mass and overall dimensions of hydraulic control devices, allowing them to be combined into blocks, and combining the functions of hydraulic units. The use of industrial water as the working fluid requires eliminating or reducing the number of precision friction pairs. The limited internal space of wheelless robots requires a special approach to cooling the units and hydraulic control systems.

The main problem in operating hydraulic control systems is contamination of the working fluid. The design features of these systems do not allow the necessary filtration equipment to be installed. Considering the above requirements for hydraulic and pneumatic control systems, high-pressure jet and vortex units are proposed as the basis for their control components. These units have no precision friction pairs and allow relatively large clearances between parts in the flow passage of the device.

Developed High-Pressure Jet and Vortex Devices Forming the Basis of the Set of Control Components

The schematic and design solutions for high-pressure jet and vortex devices allow them to operate with contaminated working fluids. The absence of small clearances between parts allows relatively large contaminant particles to pass through and prevents clogging (obliteration) (Fig. 3).

Several schematic and design solutions for jet and vortex devices have been developed. The universal high-pressure jet unit (Fig. 4) has a supply nozzle 1. To form a compact jet at the nozzle outlet, its peripheral parts are formed by control jets 3 flowing from nozzles 2. Varying the pressure P_y at the control nozzle inlet adjusts the shape and direction of the main jet, which propagates in a low-pressure chamber at $P_c \approx 0.1–0.5$ MPa. A focusing deflector 4 is located in the chamber and compresses the jet in the vertical direction.

This deflector has a wedge-shaped slot, in the plane of which a rectangular jet is formed in region 5. Moving the deflector 4 provides the required shape and position of the jet in the chamber. A control deflector 6 is installed in the chamber downstream of the focusing deflector 4. It has a focusing wall 7 and an edge 8 for deflecting the jet. To improve the stability of jet deflection, a channel 9 is formed in the deflector to supply part of the jet to the rear side of the deflector 6. Shields 10 and 11 are installed downstream of the control deflector in the low-pressure chamber. They divert the reverse flows entering the low-pressure chamber from the receiver channels.

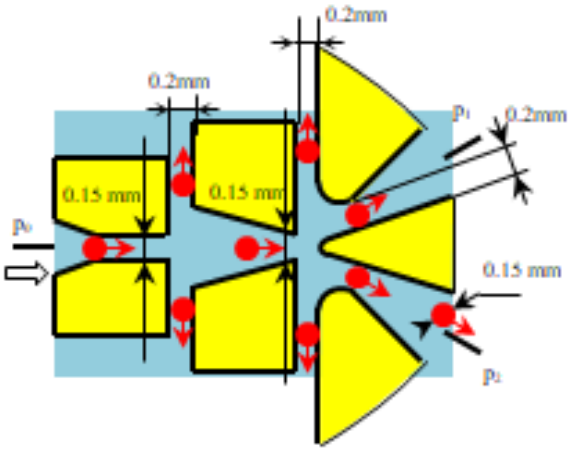


Fig. 3. Passage of particles up to 150 μm in size through the hydraulic channels of a first-stage jet amplifier.

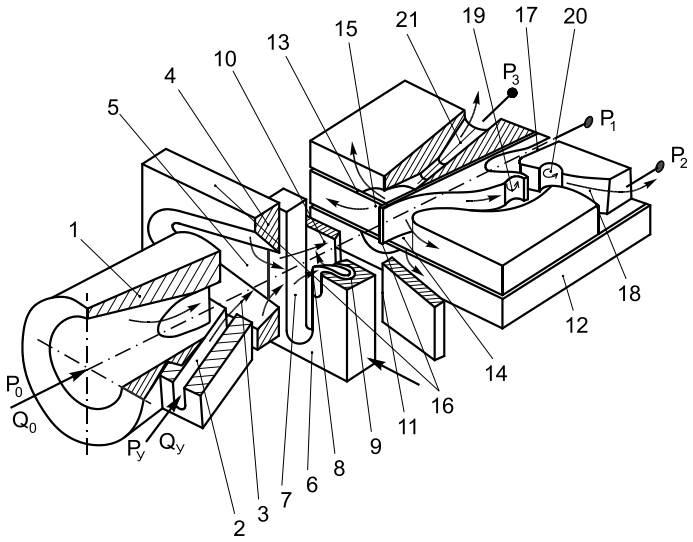


Fig. 4. Developed universal high-pressure jet unit: 1 – supply nozzle; 2 – control nozzles; 3 – control jets; 4 – focusing deflector; 5 – region of rectangular jet formation; 6 – control deflector; 7 – focusing wall; 8 – edge for jet deflection; 9 – channel supplying part of the jet to the rear side of the control deflector; 10, 11 – shields for diverting reverse flows; 12 – receiver channel block; 13 – bridges between plates; 14, 15 – main receiver channels; 16 – separating wedge; 17 – receiver channel outlet; 18 – additional receiver channel outlet; 19, 20 – recesses for flow stabilisation; 21 – additional outlets for utilising the peripheral parts of the main jet.

The kinetic energy of the jet is converted into the potential energy of the compressed fluid in the receiver channel block 12. The receiver channel block 12 contains a stack of plates separated by bridges 13. The main receiver channels 14 and 15 are formed in the central plate and separated by a wedge 16. Each receiver channel has an outlet 17 and an additional outlet 18. Recesses 19 and 20 are formed in the hydraulic line of the receiver channel to stabilise fluid flow in its branched hydraulic line. The plate stack of the receiver channel block has additional outlets 21 for utilising the peripheral parts of the main jet.

The proposed jet devices have chamber lengths ranging from 2 to 4 mm. The nozzle outlet diameters are 0.2–1.0 mm. The receiver channel dimensions are 0.3–0.8 mm. The device parts are subjected to high-pressure fluid flows with velocities reaching 200 m/s and above.

The set of control components comprises various jet devices. They have nozzles with openings of different shapes that form corresponding jets (Fig. 5a).

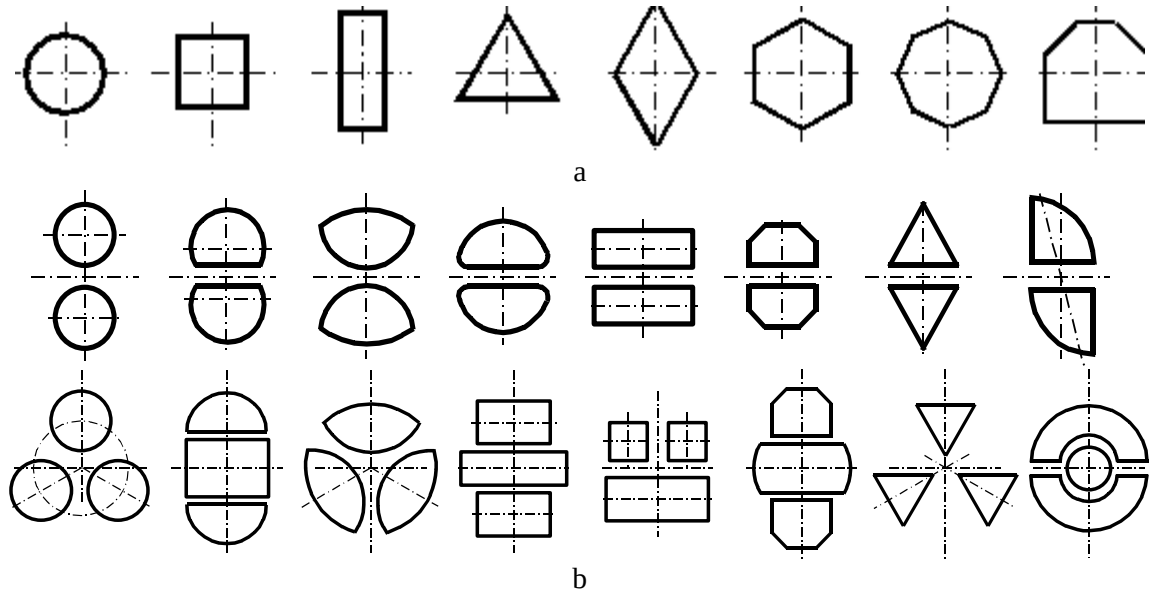


Fig. 5. Typical shapes of outlet openings: (a) small nozzle devices (approximately 1 mm in size); (b) receiver channel systems.

A symmetrical pair of receiver channels in a jet device is generally formed by two openings of identical size and shape (Fig. 5b). A system of three receiver channels can be symmetrical about two axes or have axial symmetry about three or more axes. A system of four or more receiver channels is generally arranged symmetrically about two mutually perpendicular planes. Devices with more than four receiver channels are also used.

Formation of Finite-Volume Vortex Flows and High-Pressure Vortex Devices

To improve the efficiency of high-pressure jet devices, innovative methods have been proposed for forming jets with isolated, periodic, high-pressure vortex flows of finite volume incorporated into them. These finite-volume flows take the form of a spatial dipole [28], a vortex ring, or a vortex filament.

A vortex ring is formed in an annular gap through which fluid flows. An additional pulsed fluid flow is introduced into and withdrawn from this flow (Fig. 6).

Fluid flows through the annular gap at a flow rate Q_0 (Fig. 6). Let us assume that the fluid particle velocities V_0 are parallel to the x-axis and that the velocity profile $V_0(y)$ in the annular gap is nearly uniform, with sharply varying regions at the walls corresponding to the boundary layers.

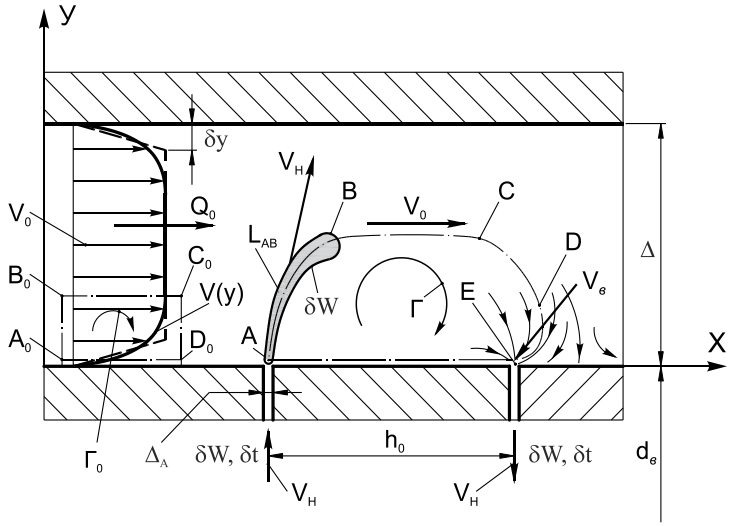


Fig. 6. Schematic diagram of the formation of an isolated vortex in an annular gap.

The presence of boundary layers gives rise to a region of vortex formation (a vortex sheet) at the walls of the annular gap. This occurs in both laminar and turbulent fluid flow. Vortex formation is most intense in the fluid layers adjacent to the solid walls. Therefore, for the selected closed contour $A_0B_0C_0D_0$ near the wall, the velocity circulation around the contour is determined by the velocity along segment B_0C_0 and is given by

$$\Gamma_0 = \oint VdL \approx V_0 \cdot B_0 \cdot C_0. \quad (1)$$

For a contour of unit length $B_0C_0 = 1$, we obtain $\Gamma_{01} = V_0 \cdot 1$.

The flux of the curl of velocity through the surface bounded by this contour is determined by the surface integral

$$\int_s rotVds = \Gamma_0 = \int_s 2\omega dS = (rotV)_0 S = 2\omega_0 \cdot S, \quad (2)$$

where S is the area of the surface bounded by the contour, $S = A_0B_0 \cdot B_0C_0$; ω_0 is the mean angular velocity of rotation of the fluid particles; and $(rotV)$ is the local value of the curl of velocity within the contour.

The circulation Γ_0 around the contour, described by equation (1), depends on the dimensions of the contour $A_0B_0C_0D_0$. In the region corresponding to the boundary layer, at small values of the contour height $A_0B_0 = C_0D_0$, the circulation increases as the velocity $V(y)$ increases. For simplicity, let us assume that the velocity profile is approximately trapezoidal within the boundary layer of thickness δy. Within the boundary layer, the velocity circulation then increases linearly, while outside it the circulation remains constant. Thus, for a contour of unit length $B_0C_0 = 1$

$$\Gamma_{01} = \begin{cases} V_0 \cdot y / \delta y & for\ y \le \delta y \\ V_0 & for\ y > \delta y \end{cases} \quad (3)$$

Thus, a steady vortex motion of the fluid exists in the annular gap. It is concentrated near the solid walls and has a stable vorticity corresponding to the velocity circulation per unit length Γ_{01}.

Let us select a toroidal control volume with a radial cross-section $ABCDE$ in the annular gap. Points A and E of this volume correspond to the positions of the outlet openings of small radial slots. Through these slots, a pulsed fluid flow of volume δW is introduced into and withdrawn from the annular gap over a time interval δt, starting at time t_0. Before time t_0, the velocity circulation around contour $A...E$ is determined solely by the flow in the annular gap and is equal to $\Gamma_0 = h_0V_0$. The sign of the circulation corresponds to the clockwise rotation of fluid particles within the selected contour, as indicated by arrow Γ.

During a short time interval δt, a fluid volume δW enters the annular gap through slot A. The mean fluid flow rate through the slot is

$$Q = \frac{\delta W}{\delta t}, \quad (4)$$

and the mean velocity of the fluid particles in the slot cross-section is

$$V_H = \frac{Q}{S_A},$$

where $S_A = \Delta_A \cdot \pi d_B$ is the cross-sectional area of the slot, Δ_A is the slot width, and d_B is the insert diameter.

The slot is oriented perpendicular to the channel wall. The fluid particles moving through the slot acquire considerable kinetic energy. As the fluid leaves the slot and enters the annular gap, it forms a fan-shaped flow AB. This flow is acted upon by a perpendicular fluid flow in the annular channel with a velocity V_0. As a result, the fan-shaped flow is deflected, and its cross-section takes a parabolic shape corresponding to curve AB. Given the short time

required for the flow to form, it can be assumed that the fluid from the slot is concentrated in a narrow region whose width differs little from the slot width Δ_A. Accordingly, the length of this region is

$$L_{AB} = \frac{\delta W}{\pi d_B \Delta_A} = \frac{\delta W}{S_A},$$

Let us assume that diffusion of the radial flow is negligible. Taking equation (4) into account, the velocity circulation along segment *AB* is then

$$\Gamma_{AB} = V_H \cdot L_{AB} = \frac{Q}{S_A} \cdot \frac{\delta W}{S_A} = \frac{\delta W^2}{S_A^2 \delta t}. \quad (5)$$

This estimate of the circulation establishes how individual parameters affect its magnitude. Equation (5) shows that increasing the circulation requires increasing the fluid volume δW, reducing the cross-sectional area of the slot, and increasing the response speed of the device supplying fluid to the slot.

This simplified approach was refined by taking into account the effect of the outflow at *E* in the annular gap. A flow model consisting of a source interacting with an incoming uniform fluid flow was used. According to this model, fluid entering slot *E* forms curved streamlines corresponding to contour *CDE*. A region of flow deceleration develops on the insert surface. Fluid entering slot *E* promotes rotational motion in the annular gap, increasing the overall vorticity of the flow.

Isolated vortices form periodically in the annular gap. As a result, a vortex system consisting of successive vortices is generated in the fluid flow. Several schematic and design solutions have been developed for devices that generate vortex systems. In particular, a design has been proposed for a jet device that forms a vortex system in the nozzle channel.

The device incorporated into the flow passage of the nozzle of a nozzle–flapper amplifier (Fig. 7) has a nozzle 1 with a conical bore and a cylindrical outlet section of diameter d_c. A sleeve 2 is located in the central part of the nozzle and is secured axially by a cover 3. The nozzle mounting bore of diameter $d_П$, together with the outer surface of the sleeve, forms an annular nozzle 4 and an annular receiver channel 5 of the jet device. Fluid is supplied to the annular nozzle through hydraulic line 6 at pressure P_H. A pressure P_K develops at the outlet of channel 5 of the jet device. This pressure is determined, in particular, by the volume of the outlet cavity 7. Pressure P_K reaches its maximum value P_H when the distance between the outlet of annular channel 4 and the inlet of receiver channel 5 does not exceed four times the slot width of channel 4.

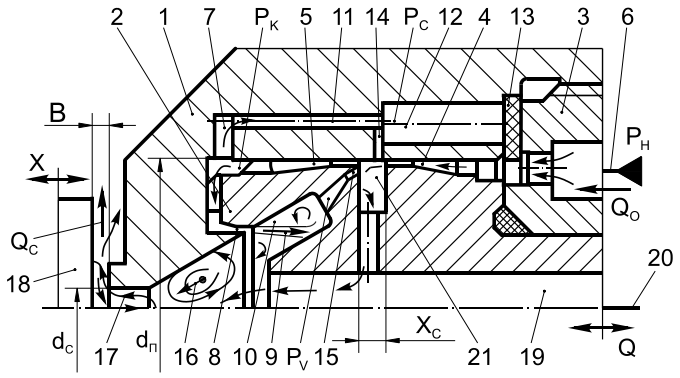


Fig. 7. Design scheme of a vortex device incorporated into the flow passage of the nozzle of a nozzle–flapper amplifier: 1 – nozzle; 2 – sleeve; 3 – cover; 4 – annular nozzle; 5 – annular receiver channel; 6 – fluid supply line; 7 – outlet cavity; 8 – vortex-forming nozzle; 9 – fluid jet; 10 – conical vortex chamber; 11 – capillary channels; 12 – cavity; 13 – sealing gasket; 14 – control channel; 15 – annular outlet channel; 16 – direction of vortex movement; 17 – quasi-steady flow at the nozzle outlet and on the flapper surface; 18 – flapper; 19 – outlet opening; 20 – hydraulic line connecting to the second-stage amplifier; 21 – jet device chamber.

Fluid from cavity 7 enters the vortex-forming nozzle 8 (Fig. 7). The fluid jet 9 leaving nozzle 8 creates a vortex flow with positive circulation in the conical vortex chamber 10. At the same time, fluid from cavity 7 passes through capillary channels 11 into cavity 12, which is sealed by a deformed gasket 13. The inertia of the fluid in capillary channels 11 and the compression of the fluid in cavity 12 cause a delay in the pressure rise P_c in cavity 12. As pressure P_c rises in control channel 14 of the jet device, the jet leaving annular nozzle 4 is deflected. The jet then enters annular outlet channel 15 instead of receiver channel 5.

An excess pressure P_V develops at the outlet of channel 15 and exerts a force on the vortex formed in vortex chamber 10. Deflection of the jet leaving nozzle 4 causes pressure P_K to drop at the outlet of receiver channel 5 in cavity 7. The presence of compressed fluid in cavity 7 somewhat slows this pressure drop. As pressure P_K in cavity 7 decreases, the flow in nozzle 8 and jet 9 slows down. Under the action of pressure P_V, the vortex is expelled from chamber 10. It travels along the nozzle wall in the flow direction indicated by arrow 16.

Due to the inertia of the fluid in capillary channels 11 and the compression of the fluid in cavity 12, pressure P_c in control channel 14 decreases with a certain delay. This ensures that the vortex formed in chamber 10 is completely expelled from the chamber. After the vortex is expelled, the control pressure P_c drops to zero, and the fluid jet from annular channel 4 again enters receiver channel 5, creating an excess pressure P_K at its outlet in cavity 7. The cycle of vortex formation in chamber 10 then repeats.

The nozzle design described above is used in a nozzle–flapper device. The resulting vortex ring moves along the wall of nozzle 1 in direction 16. As the vortex moves through the cylindrical section of the nozzle, it transforms into a high-pressure flow of ellipsoidal shape. This ellipsoidal flow merges with flow 17, which is in a quasi-steady state at the outlet opening and on the surface of flapper 18. The flows merge and undergo transformation.

Thus, flow 17 exists in a quasi-steady state in the gap between nozzle 1 and flapper 18. It reduces the effective flow area of the opening in nozzle 1 and, consequently, reduces the mean flow rate Q_c through the nozzle–flapper device.

The reduction in the mean flow rate through the nozzle is equivalent to a reduction in its cross-sectional area. It was established that the flow rate decreases by a factor of 1.6–1.7. Accordingly, at equal flow rates, a nozzle in which vortex systems are generated has a diameter 2.5–2.8 times that of a nozzle in a device without vortices.

For example, a nozzle with a diameter d_c = 0.5 mm in the presence of vortices is equivalent to a nozzle with a diameter d_c = 0.3 mm used in existing nozzle–flapper devices. Increasing the diameter leads to a corresponding increase in the gap B between the nozzle end face and the flapper. This substantially reduces the sensitivity of the device to contaminants in the working fluid.

The nozzle has an outlet opening 19 connected to the second-stage amplifier through hydraulic line 20. The pressure P and flow rate Q in this line are the nozzle output parameters, which depend on the displacement x of flapper 18. Given the high frequency of vortex formation and passage through the nozzle opening, the output parameters P and Q remain practically constant over time (quasi-static). The proposed device design essentially combines a throttle and a nozzle–flapper device. Annular nozzle 4 acts as the throttle. The pressure in chamber 21 of the jet device is practically the same as the output pressure P.

This provides a nozzle–flapper device in which the fluid flow contains periodic high-pressure vortex flows of finite volume.

A specific feature of this device is its considerably lower sensitivity to working fluid contamination. An additional advantage is its reliable operation at low temperatures. Increasing the minimum flow area of the nozzle improves the reliability of the device when the working fluid thickens at low temperatures. The jet components of hydraulic control systems require optimal geometry of the flow passages in the jet devices. The geometry was optimised on the basis of studies of the fluid flow processes.

Study of the Features of Hydrodynamic Working Processes in Jet Devices of Hydraulic Control Systems

The working processes were studied through numerical flow calculations supplemented by a wide range of experimental studies. The calculations were performed by integrating the Navier–Stokes equations using the finite element method [28]. The flow patterns in a deflector-type jet device were determined (Fig. 8).

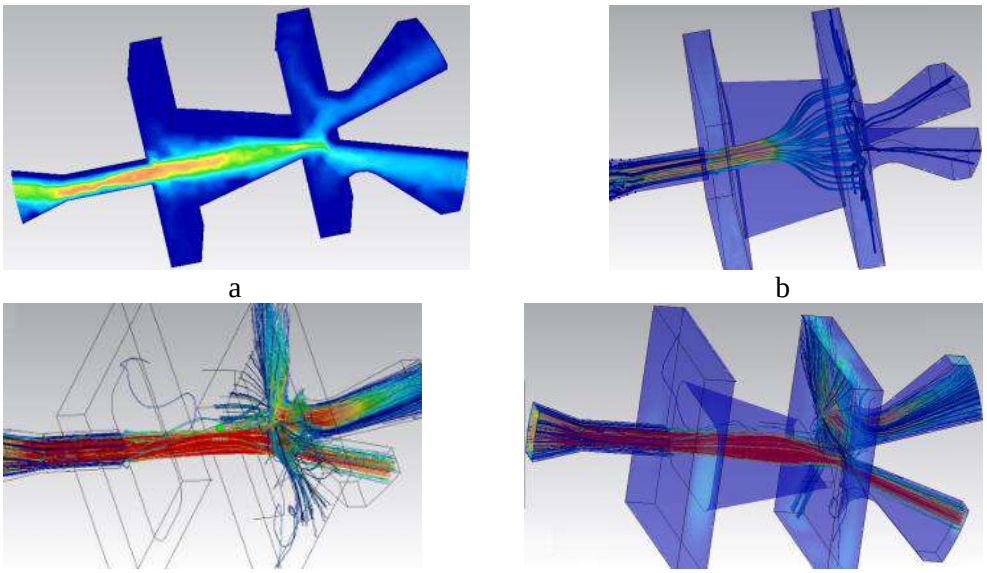


Fig. 8. Results of numerical flow calculations for a deflector-type jet device: (a) distribution of the fluid particle velocity magnitude in the plane of symmetry of the device; (b) streamline pattern during jet deflection by the deflector; (c) trajectories of individual fluid particles in the region between the deflector and the receiver channels; (d) overall visualisation of the three-dimensional flow.

The calculations showed that the compact jet at the nozzle outlet exhibits static instability (Fig. 8a). This is caused by the presence of a section of constant cross-sectional area at the nozzle outlet. The boundary layers developing along the walls of this section narrow the uniform-velocity core of the flow at the nozzle outlet. The numerical calculations revealed specific features of the working processes, particularly the deformation of the jet as it interacts with the deflector surface (Fig. 8b). When the jet interacts with the receiver channels, which allow through-flow in these calculations, reverse flows from the channels into the chamber are observed (Fig. 8c).

The calculations showed that the deformed jet has low-power peripheral regions that do not enter the receiver channels but spread over the end face. Analysis of the fluid particle trajectories in the three-dimensional flow within the jet device indicates the presence of fluid flows in different directions in the region between the deflector and the receiver channels (Fig. 8d).

The numerical calculations identified qualitative features of the working processes and characteristic flow regions that were subsequently studied in greater detail. These include the jet flow at the nozzle outlet, the interaction of the jet with the deflector, the flow in the receiver channels, and the reverse flows formed in the receiver channels. All these regions contain singular flow regions where the stress tensor and the rate-of-strain tensor become degenerate.

Singular Flow Regions

The analysis of singular regions is based on experimental flow studies using visualisation in a planar model device. In particular, a jet entering a chamber was studied. The jet entrains the surrounding fluid in the chamber and expands (Fig. 9a).

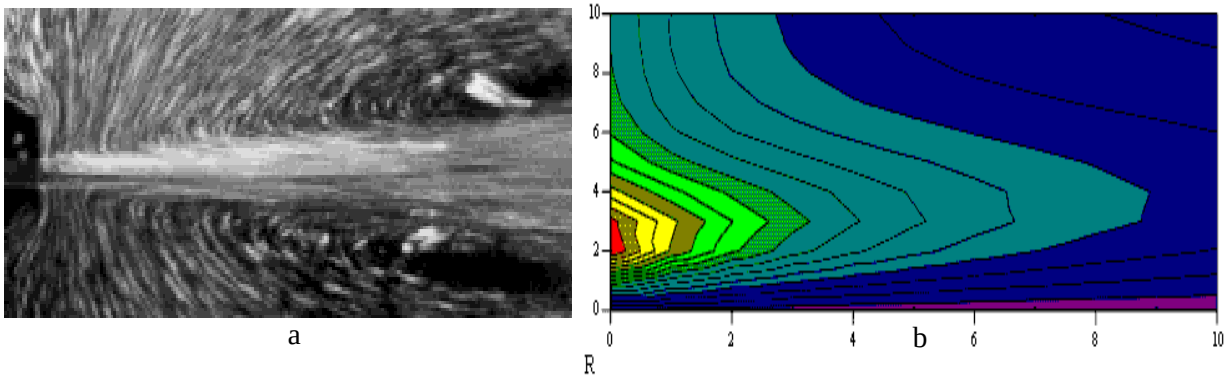


Fig. 9. Experimental flow visualisation: (a) flow around a jet propagating in a chamber; (b) calculated distribution of the magnitude of the curl of velocity at the jet boundary, represented by vorticity contours.

A specific feature of the flow is the singular region at the nozzle edge. In this region, the stress tensor and the rate-of-strain tensor become degenerate. In the experiments, this manifests itself in vortex and cavitation phenomena near the nozzle edge. The calculated value of vorticity (the curl of velocity) was used to quantitatively assess changes in the hydrodynamic parameters of the fluid in this region (Fig. 9b).

The flow in the singular region was studied analytically.

The following method was developed for analysing differential equations at singular points. At a singular point, the fluid particle velocity vector $\vec{v} \cong 0$, and, accordingly, the velocity components along the coordinate axes *x*, *y*, and *z* are:

$$v_x \cong v_y \cong v_z \cong 0.$$

The velocity components are functions of the coordinates:

$$\frac{dx}{dt} = v_x(x,y,z),\ \frac{dy}{dt} = v_y(x,y,z),\ \frac{dz}{dt} = v_z(x,y,z). \tag{6}$$

Let us expand functions (6) in a Taylor series, retaining the linear terms:

$$\begin{aligned} v_x &= \varepsilon\left(\frac{\partial v_x}{\partial x}\right)\Big|_0 x + \varepsilon\frac{\partial v_x}{\partial y}\Big|_0 y + \varepsilon\frac{\partial v_x}{\partial z}\Big|_0 z + 0(\varepsilon) \\ v_y &= \varepsilon\left(\frac{\partial v_y}{\partial x}\right)\Big|_0 x + \varepsilon\frac{\partial v_y}{\partial y}\Big|_0 y + \varepsilon\frac{\partial v_y}{\partial z}\Big|_0 z + 0(\varepsilon)\ \ (\varepsilon \to 0). \\ v_z &= \varepsilon\left(\frac{\partial v_z}{\partial x}\right)\Big|_0 x + \varepsilon\frac{\partial v_z}{\partial y}\Big|_0 y + \varepsilon\frac{\partial v_z}{\partial z}\Big|_0 z + 0(\varepsilon) \end{aligned} \tag{7}$$

The matrix of coefficients of series (7) has the form:

$$K = \begin{vmatrix} \frac{\partial v_x}{\partial x}\Big|_0 & \frac{\partial v_x}{\partial y}\Big|_0 & \frac{\partial v_x}{\partial z}\Big|_0 \\ \frac{\partial v_y}{\partial x}\Big|_0 & \frac{\partial v_y}{\partial y}\Big|_0 & \frac{\partial v_y}{\partial z}\Big|_0 \\ \frac{\partial v_z}{\partial x}\Big|_0 & \frac{\partial v_z}{\partial y}\Big|_0 & \frac{\partial v_z}{\partial z}\Big|_0 \end{vmatrix}. \tag{8}$$

The rate-of-strain tensor of the fluid $\dot{S}$ [28] is defined as:

$$\dot{S} = \begin{bmatrix} \frac{\partial V_x}{\partial x} & \frac{1}{2}\left(\frac{\partial V_y}{\partial x} + \frac{\partial V_x}{\partial y}\right) & \frac{1}{2}\left(\frac{\partial V_z}{\partial x} + \frac{\partial V_x}{\partial z}\right) \\ \frac{1}{2}\left(\frac{\partial V_x}{\partial y} + \frac{\partial V_y}{\partial x}\right) & \frac{\partial V_y}{\partial y} & \frac{1}{2}\left(\frac{\partial V_z}{\partial y} + \frac{\partial V_y}{\partial z}\right) \\ \frac{1}{2}\left(\frac{\partial V_x}{\partial z} + \frac{\partial V_z}{\partial x}\right) & \frac{1}{2}\left(\frac{\partial V_y}{\partial z} + \frac{\partial V_z}{\partial y}\right) & \frac{\partial V_z}{\partial z} \end{bmatrix}. \quad (9)$$

Let us assume that the fluid flow in the singular region is irrotational. Accordingly:

$$rot\vec{V} = 0. \quad (10)$$

From (10), we obtain the relations:

$$\frac{\partial V_z}{\partial y} = \frac{\partial V_y}{\partial z}, \quad \frac{\partial V_x}{\partial z} = \frac{\partial V_z}{\partial x}, \quad \frac{\partial V_y}{\partial x} = \frac{\partial V_x}{\partial y}. \quad (11)$$

Substituting (11) into (9), we obtain the matrix of the rate-of-strain tensor in the form:

$$\dot{S}_{\omega=0} = \begin{bmatrix} \frac{\partial V_x}{\partial x} & \frac{\partial V_x}{\partial y} & \frac{\partial V_x}{\partial z} \\ \frac{\partial V_y}{\partial x} & \frac{\partial V_y}{\partial y} & \frac{\partial V_z}{\partial z} \\ \frac{\partial V_z}{\partial x} & \frac{\partial V_z}{\partial y} & \frac{\partial V_z}{\partial z} \end{bmatrix}. \quad (12)$$

Comparison of matrices (8) and (12) shows that matrix K corresponds to the matrix of components of the rate-of-strain tensor $\dot{S}$.

For a Newtonian fluid, there is a linear relationship between the stress tensor P and the rate-of-strain tensor $\dot{S}$:

$$P = a\dot{S} + bE,$$

where a and b are scalars; $\mathbf{a} = 2\mu$, where μ is the dynamic viscosity of the fluid; and E is the identity tensor.

Therefore, degeneracy of the rate-of-strain tensor corresponds to degeneracy of the stress tensor.

To determine the principal components of the rate-of-strain tensor $\dot{S}$, which correspond to the eigenvalues of the matrix, we obtain the characteristic equation:

$$\det\left|A - \lambda E\right| = 0, \quad (13)$$

where E is the identity matrix.

The coefficients of equation (13) do not depend on the choice of coordinate system and are invariants of the rate-of-strain tensor $\dot{S}$.

Let us analyse the eigenvalues of matrix K, which coincide with the principal components of the rate-of-strain tensor (12) and, accordingly, of the stress tensor in the fluid. If all eigenvalues are positive, $\lambda_1 > 0$, $\lambda_2 > 0$, $\lambda_3 > 0$, an unstable node is obtained. If $\lambda_1 > 0$, $\lambda_2 < 0$, $\lambda_3 < 0$, a three-dimensional flow of the stable saddle type occurs. This type of flow occurs in the singular region at the nozzle edge. In this region, fluid from the jet and the surroundings moves in the z-direction (Fig. 10a).

An elementary fluid particle flowing near a stable saddle is deformed (Fig. 10b) and loses its continuity due to cavitation. More complex singular regions occur in the receiver channels

(Fig. 10c). Singular regions largely determine the overall flow parameters in jet devices. These regions were identified through experimental studies.

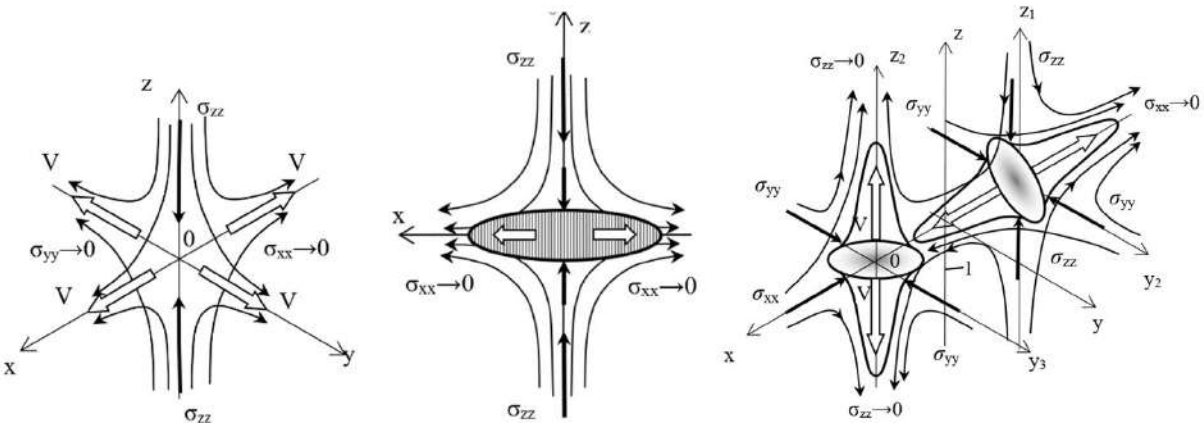


Fig. 10. Schemes of flow and fluid particle deformation in singular regions: (a) three-dimensional representation of a stable saddle-type flow near the nozzle edge when the stresses σxx and σyy instantaneously drop to zero; (b) deformation of a fluid particle in this region; (c) scheme of deformation of elementary fluid particles in a singular region corresponding to two mutually perpendicular lines of expansion.

Experimental Flow Studies and Features of the Working Processes in Jet Devices

The interaction of the jet with the deflector produces a complex flow pattern with vortex zones 2 and critical points 3 and 4 on the deflector walls (Fig. 11a).

The jet is compressed, forming jet 5, and intense reverse flows develop, bounded by streamlines 6, 8 and 7, 9. Flows 10 initiate vortex zones 11. Jet compression causes deformation of the outlet velocity profile. In the two-dimensional problem considered, the fluid particles accelerate near the deflector walls. This is reflected in changes in velocity profile 12.

The calculation results were confirmed experimentally (Fig. 11b). The photograph shows singular regions of the stable saddle type that occur on the deflector walls.

The three-dimensional flow in the region of interaction between the jet and the deflector was studied experimentally. It was established that the interaction of a round or square jet with a flat deflector changes the jet shape to an elliptical (oval) form. The jet dimensions in the direction perpendicular to the deflector edge increase by a factor of 2–3.

Theoretical (Fig. 12a) and experimental studies of the interaction between the jet and the receiver channel were carried out.

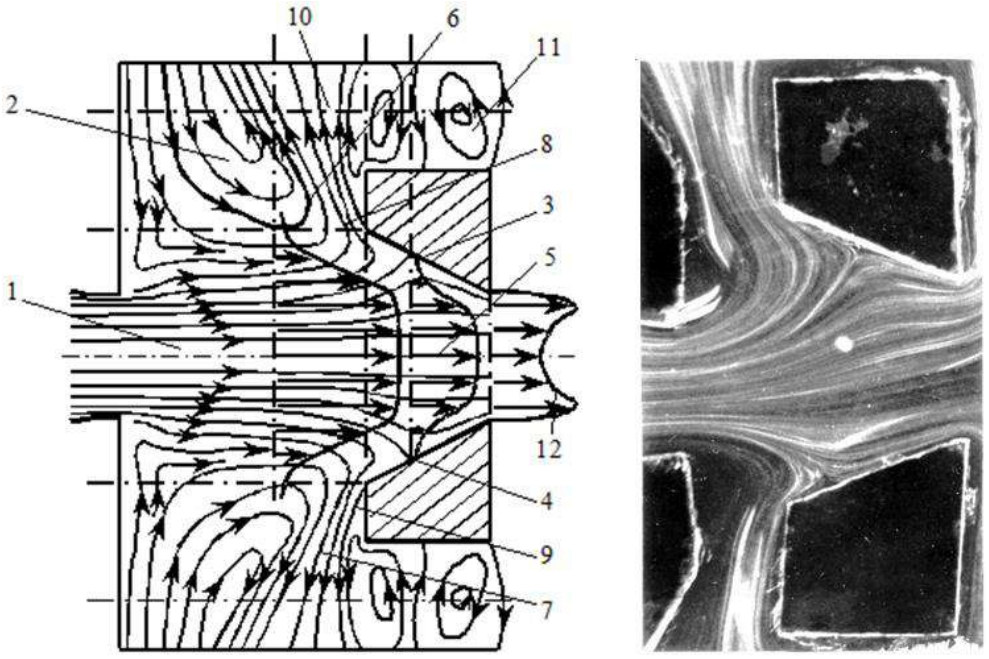
Jet 1 entering the channel initiates an opposing fluid flow 2. The jet turns in region 3, forming reverse flows 4 outside the channel. Vortex regions 5 form in the receiver channel. At the channel inlet, velocity profile 6 changes sign, and the net fluid flow rate through the inlet cross-section is zero. A singular flow region of the stable saddle type occurs at the interface between flows 1 and 2 in the centre of the channel (Fig. 10a).

The calculated flow pattern was confirmed experimentally (Fig. 12b). The singular region manifests itself in the almost complete stopping of fluid particles.

The interaction of a jet with two receiver channels was studied, including by experimental methods. Intense vortex formation occurs in the flow passages of the receiver channels, where singular flow regions are also present (Fig. 13a).

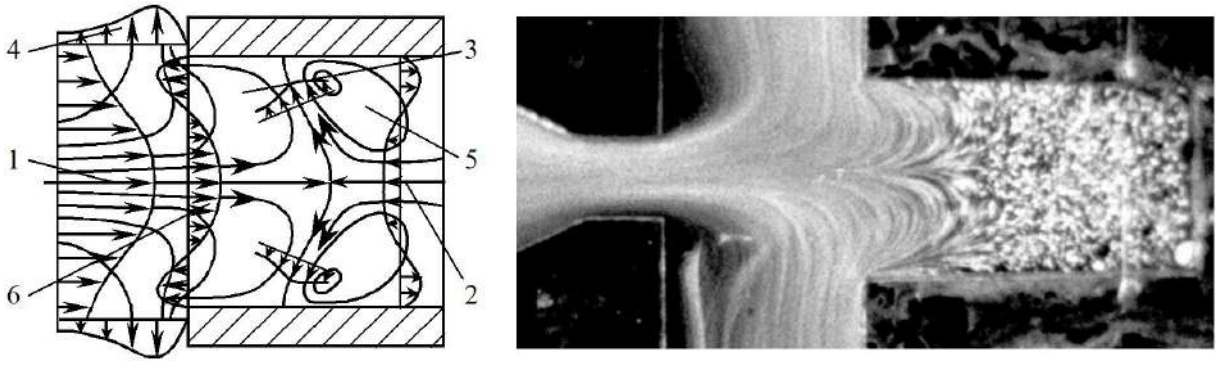
Singular flow regions corresponding to the intersection of two mutually perpendicular lines of expansion occur at the edges of the receiver channels (Fig. 10c).

Non-circular turbulent jets are mainly used in high-pressure jet devices. These jets were studied experimentally (Fig. 14).



a b

Fig. 11. Interaction of a jet with a converging deflector: (a) calculated streamlines and velocity profiles; (b) photograph of the visualised flow in the model device; 1 – incoming jet; 2 – vortex zones; 3, 4 – critical points on the deflector walls; 5 – compressed jet; 6, 8 and 7, 9 – streamlines bounding the reverse flows; 10 – flows initiating vortex zones 11; 12 – velocity profile at the deflector outlet.



a b

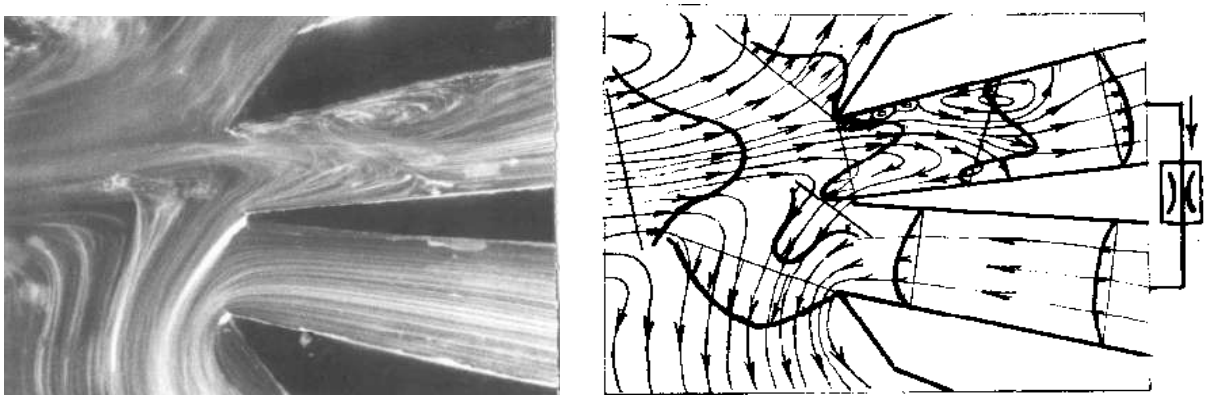
Fig. 12. Interaction of a jet with a receiver channel without through-flow: (a) calculated streamline pattern and velocity profiles; (b) photograph of the visualised flow; 1 – incoming jet; 2 – opposing fluid flow; 3 – region where the jet turns; 4 – reverse flows outside the channel; 5 – vortex regions in the receiver channel; 6 – velocity profile with a change of sign at the channel inlet.

The nature of the flow determines the device characteristics and the surface wear of its parts. The flow features were identified from the surface wear of the parts, and a three-dimensional diagram of the fluid flows in the region where the jet enters the receiver channels was constructed (Fig. 15).

The oval jet *Sc* formed at the deflector outlet splits into two forward flows Π_N and Π_V, which are associated with two symmetrical parts of the vortex filaments Ω_1 and Ω_2 formed in the jet deflected by the deflector. The intensity of vortex filaments Ω_1 and Ω_2 is low, and the helical motion in flows Π_N and Π_V rapidly decays. The upper forward flow Π_V and the lower forward flow Π_N enter receiver channels 2 and 1, respectively, penetrate to a small depth, and then turn back, forming a system of three-dimensional reverse flows.

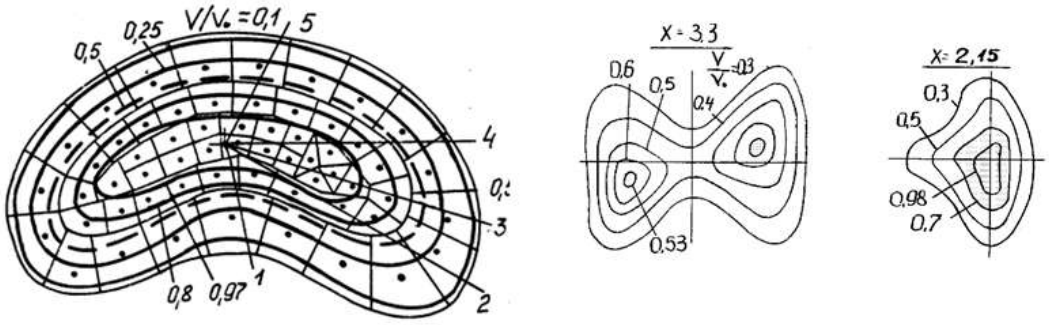
The lower forward flow Π_N forms two localised forward flows P_{N1} and P_{N2} in receiver channel 1. These flows then spread over the surface of the lower sleeve W_N, causing abrasive

wear and forming wear recesses V_{N1} and V_{N3} on the surface. Reverse flows Z_{N2} and Z_{N4} are similarly formed in channel 1.



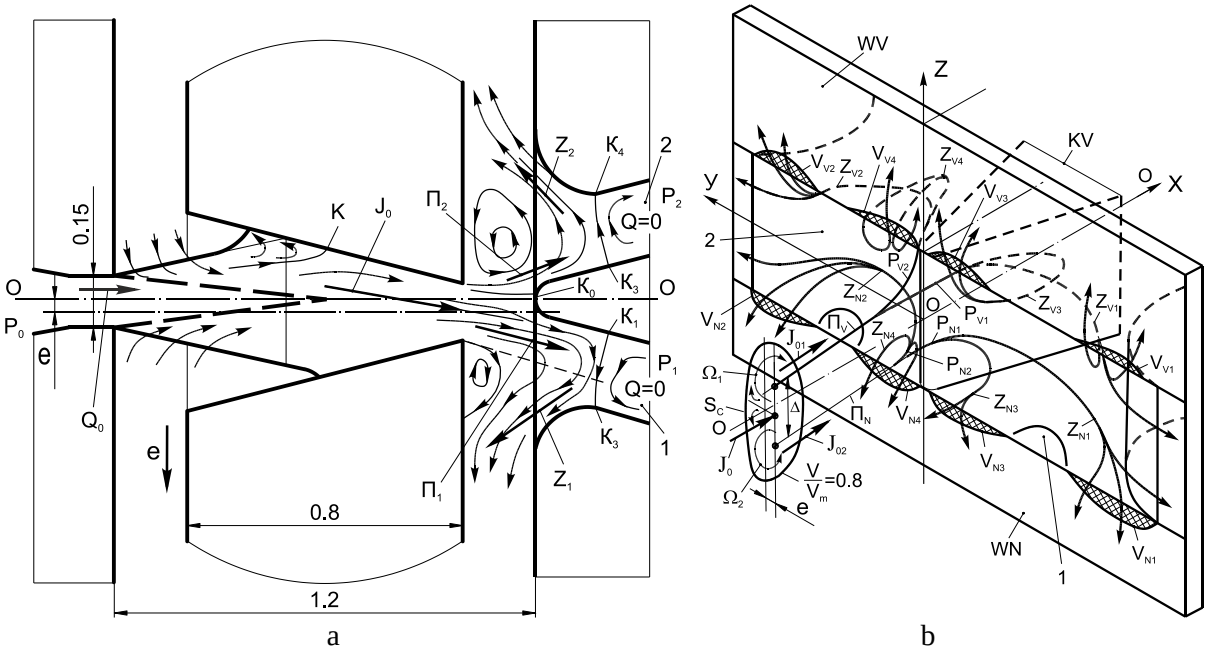
a b

Fig. 13. Interaction of a jet with two receiver channels: (a) photograph of the visualised flow; (b) corresponding diagram of streamlines and velocity profiles.



a b c

Fig. 14. Results of experimental measurements of velocity distributions in the cross-sections of non-circular turbulent jets: (a) segment-shaped jet; (b) pair of jets; (c) T-shaped jet.



a b

Fig. 15. Flow diagram in the middle cross-section of the jet device (a) and locations of three-dimensional flows at the end face of the receiver channels, determined from surface wear (b); Sc – oval jet at the deflector outlet; ПN, ПV – lower and upper forward flows; Ω₁, Ω₂ – vortex filaments; PN1, PN2, PV1, PV2 – localised forward flows; ZN1–ZN4, ZV1–ZV4 – reverse flows; VN1–VN4, VV1–VV4 – surface wear regions; WN, WV – lower and upper sleeves; KV – wedge-shaped protrusion; O – region in the middle part of the protrusion.

The upper forward flow $П_V$ of jet S_c also splits into P_{V1} and P_{V2}, which subsequently turn back as reverse flows Z_{V1}, Z_{V3}, Z_{V4} and Z_{V2}. These reverse flows form wear regions V_{V1}, V_{V3}, V_{V4} and V_{V2}. The reverse flows near the tip of the wedge-shaped protrusion K_V, namely Z_{N3}, Z_{N4}, Z_{V3} and Z_{V4}, act not only on the surfaces of sleeves W_V and W_N but also on the edge of the wedge-shaped protrusion K_V. Therefore, the tip of the wedge-shaped protrusion is worn over its entire height. In the middle part of the protrusion (region O), in addition to the reverse flows, forward flows $П_N$ and $П_V$ act on the wedge tip. The tip divides these flows into P_{N1} and P_{N2}, and P_{V1} and P_{V2}.

The forward and reverse flows shown in the figure form cyclically in accordance with the cyclic movement of the deflector. The total number of cycles was 10 million. Therefore, the surface wear of the jet device parts results from the cumulative action of the entire system of high-pressure jets and flows occurring in the region of the receiver channels. Accordingly, the identified three-dimensional flow diagram represents an integrated average flow pattern corresponding to the fluid flow in the jet device averaged over the cycles.

The results of the working process studies provided the basis for determining the static characteristics of the jet devices.

Static Characteristics of Jet Devices

The characteristics were determined theoretically by solving the equations of fluid mechanics in integral form [28]. In its general form, the energy characteristic relates the pressures and flow rates at the device outlet and inlet:

$$\frac{p}{p_0} = \frac{p_m}{p_0} + \frac{p_m \cdot V}{k_3} \cdot V_0 \cdot p_m \cdot s_0 \cdot \frac{Q}{p_0 \cdot V_m \cdot Q_0} + k_4 \cdot \left(\frac{s_0 \cdot Q}{s \cdot Q_0} \right)^2, \quad (14)$$

where the constants depend on the device parameters.

In fully developed turbulent flows, energy losses depend mainly on the square of the velocity. Therefore, characteristic (14) takes the form:

$$\frac{p}{p_0} = \frac{p_m}{p_0} - k_2 \cdot \left(\frac{s_0 \cdot Q}{s \cdot Q_0} \right)^2. \quad (15)$$

Calculations using relationship (15) agree with the experimental data to within 5–8% for jet devices with different shapes of receiver channel openings (Fig. 16a, b).

The energy characteristics show saturation in the outlet fluid flow rate. This is caused by the limited energy of the jet formed in the nozzle and by cavitation processes in the receiver channels. If the ratio of the receiver channel area to the nozzle area is less than 2, the maximum pressure in the receiver channels reaches the pressure at the nozzle inlet.

It was established that jet devices remain operational when fluid flows out of the receiver channel at a rate exceeding the nozzle flow rate. This occurs during braking of the hydraulic drive actuators. The static characteristics of jet devices under these outflow conditions were determined for receiver channels of different sizes (Fig. 16c).

When the receiver channel area is limited, the device outlet pressure remains stable in the presence of outflow. Increasing the receiver channel area changes the shape of the characteristic. This leads to a change in the nature of the flow.

The shape of the characteristics depends on the dimensions and shape of the jet interaction chamber. Increasing the chamber length changes the shape of the characteristic (Fig. 16d). A chamber length of no more than eight times the nozzle size is recommended.

The control characteristics of the jet device were determined in terms of the outlet flow rate at zero outlet pressure and the outlet pressure at zero flow rate (Fig. 17a, b).

The flow-rate control characteristics of the device (Fig. 17b) depend only slightly on the deflector shape and are described by the expressions:

$$\frac{Q}{Q_m} = EXP\left[-\chi_Q \cdot \left(\frac{y_\partial}{d_0}\right)^2\right], \quad \frac{p}{p_m} = EXP\left[-\chi_p \cdot \left(\frac{y_\partial}{d_0}\right)^2\right]. \qquad (16)$$

where the constant values are χ_Q = 11.0–16.0 and χ_p = 10.0–15.0.

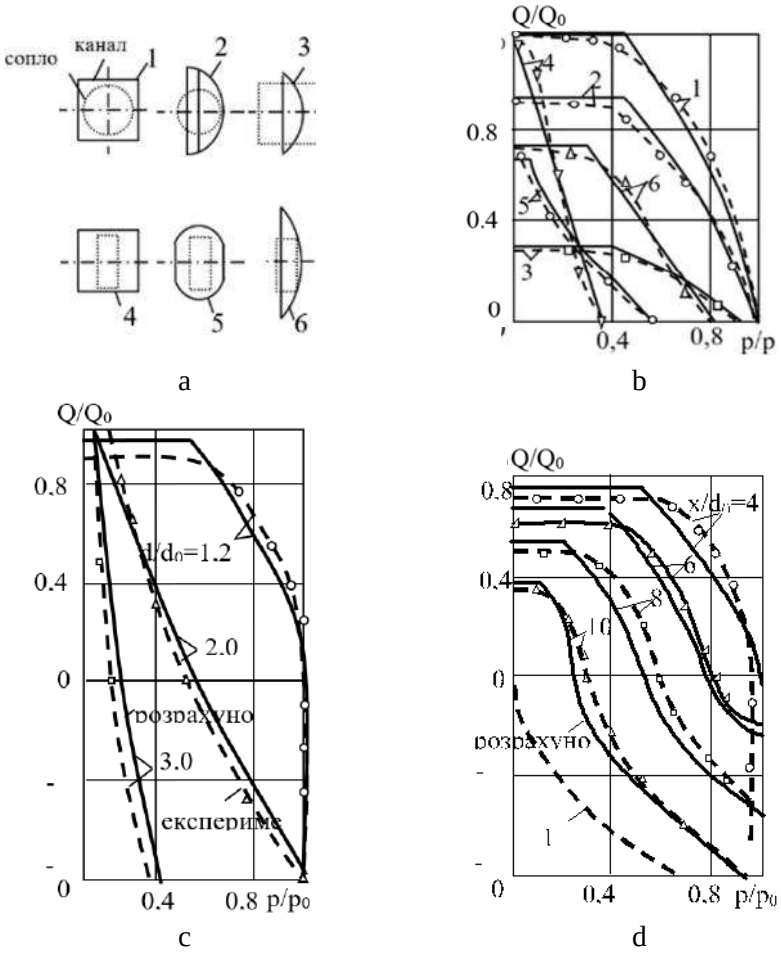


Fig. 16. Schemes of jet devices with different nozzle and receiver channel shapes (a) and the corresponding energy characteristics: (b) device energy characteristics (curves 1–6), with the curve numbers corresponding to the receiver channel shapes numbered in diagram (a); (c) energy characteristics of a jet device with a flow rate that changes sign, for different ratios of receiver channel diameter to nozzle diameter; (d) effect of the jet interaction chamber length on the energy characteristics of the jet device.

The energy characteristics of the devices (Fig. 18), measured at different fixed deflector positions, are affinely similar and correspond to the characteristic of the basic device.

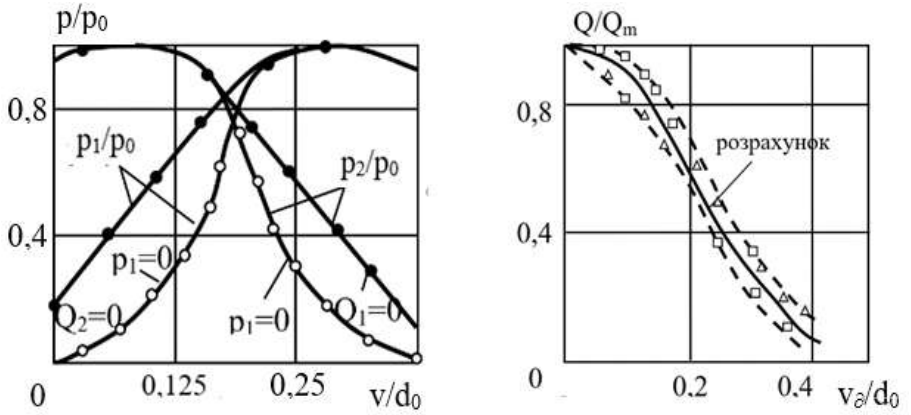
High-pressure jet devices were tested with different working media. It was established that their characteristics (14), (15), and (16) are practically independent of the chemical composition of the fluid. The tests were carried out using AMG-10 working fluid, which is typical of aircraft hydraulic drive systems.

Reliable operation of the jet devices was observed when industrial water and aqueous detergent solutions used for flushing hydraulic systems were employed as working fluids. Therefore, jet devices are recommended as components of hydraulic control systems for wheelless ground robotic complexes.

Dynamic Characteristics of Jet Devices

The dynamics of jet and vortex devices are determined by complex processes occurring in different frequency ranges. The jet device itself is a high-frequency device characterised by stochastic variations in its parameters. The dynamic properties of the jet device were studied

theoretically and experimentally. A special dynamic model accounting for the presence of undissolved air in the fluid was used (Fig. 19).



a b

Fig. 17. Control characteristics of the jet device: (a) receiver channel pressures as functions of nozzle displacement; (b) outlet flow rate as a function of deflector displacement.

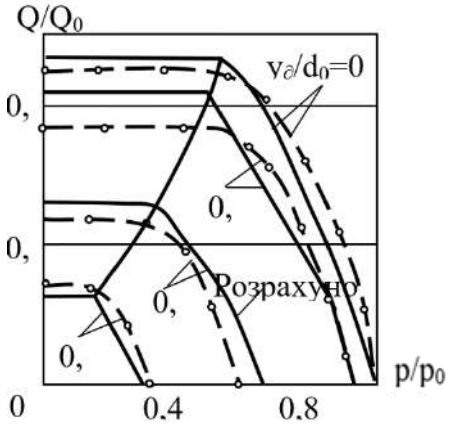


Fig. 18. Energy characteristics of the jet device at different fixed deflector positions.

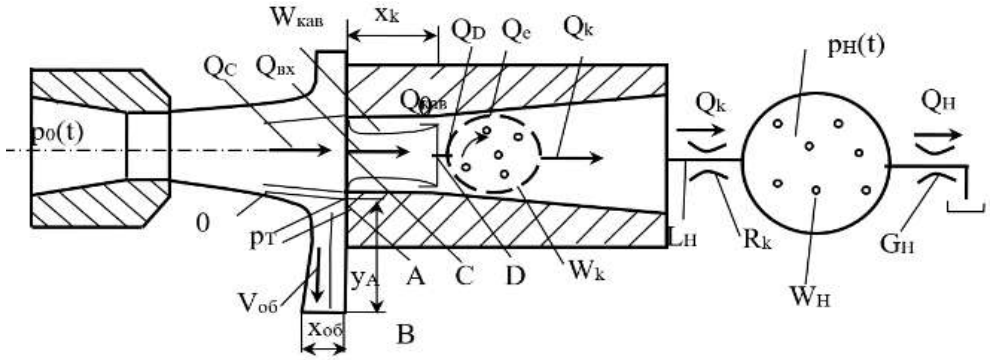


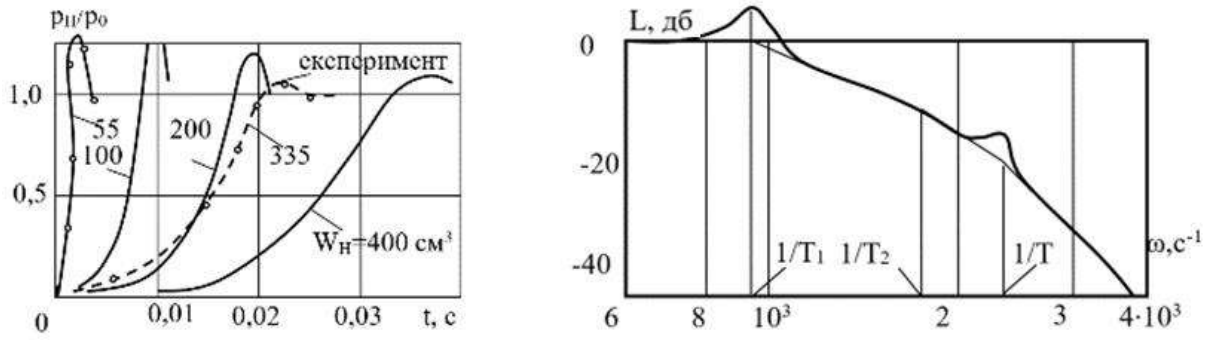
Fig. 19. Dynamic model of a jet device with a hydraulic capacitance load.

The overall transfer function of the system was determined using the dynamic model:

$$W_p(s)=\frac{p(s)}{p_0(s)}=\frac{k\cdot k_0\cdot(1-T_3\cdot s)\cdot(1-T_7\cdot s)}{(T_1\cdot s+1)\cdot(T_2^2\cdot s^2+2\xi\cdot T_2\cdot s+1)\cdot(T_3\cdot s+1)(T_8^2\cdot s^2+2\xi_k\cdot T_8\cdot s+1)}, \quad (17)$$

where s is the Laplace operator.

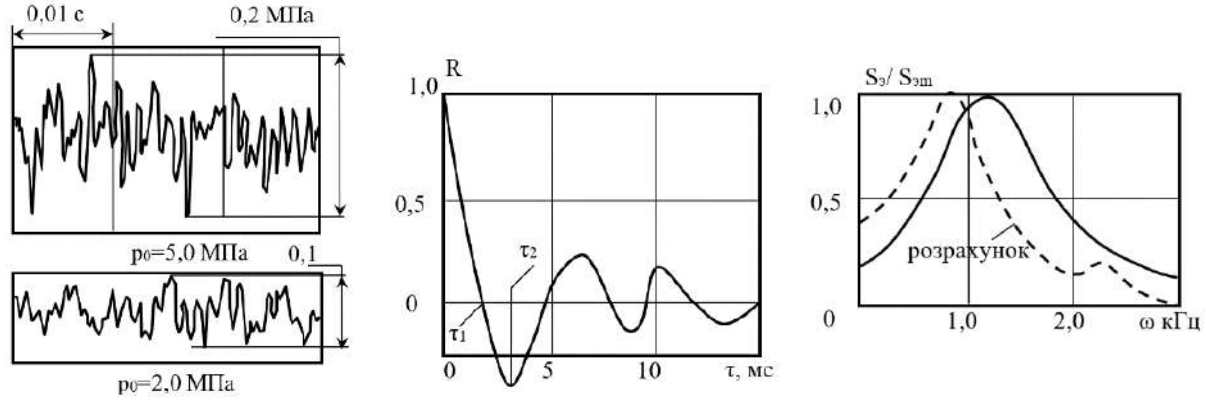
The frequency characteristics and transient responses were obtained from transfer function (17) (Fig. 20a), and the logarithmic amplitude–frequency characteristic of the jet device with a blocked receiver channel was plotted (Fig. 20b).



a b

Fig. 20. Dynamic characteristics of the jet device: (a) transient responses for different volumes of the hydraulic capacitance load; (b) logarithmic amplitude–frequency characteristic of the device with a blocked receiver channel.

Experimental studies of the dynamics were carried out using high-precision pressure sensors. Stochastic pressure fluctuations at the jet device outlet were determined (Fig. 21a).



a b c

Fig. 21. Pressure fluctuations in a chamber connected to the jet device outlet and their statistical characteristics: (a) oscillographic records at supply pressures p_0 = 5.0 MPa (upper trace) and p_0 = 2.0 MPa (lower trace); (b) correlation function; (c) spectral density of pressure fluctuations.

The experimental measurement results were processed using statistical methods and specialised software. Assuming that the random pressure fluctuations were stationary and ergodic, the correlation function (Fig. 21b) and the spectral density of the process (Fig. 21c) were determined by processing the oscillographic records.

The study results indicate that the high-pressure jet device has resonant frequencies of approximately 1 kHz. A chamber with a volume of 100 cm³ connected to the device outlet reduces the resonant frequency to 100 Hz.

Technological Features of the Design and Manufacture of Jet and Vortex Devices for Hydraulic Control Systems

High-pressure hydraulic jet devices are extremely small and are subjected to dynamic flows of fluid containing considerable contamination. Therefore, their flow passages are subject to wear. The effects of cavitation add to the dynamic action of the flow. Accordingly, these components require special techniques for machining the flow passages of jet devices. A number of design and manufacturing approaches have been proposed for producing nozzles with opening cross-sectional dimensions of 0.1–1 mm. Nozzles with non-circular openings are manufactured by plastic deformation or fitted with special cover plates (Fig. 22).

When necessary, small nozzles are assembled from separate parts (Fig. 23a). The flow passage of this nozzle is formed by wedge-shaped plates 3 pressed into body 1. At the nozzle ends, the plates are sealed with polymer 2. A cavity 4 is formed between the plates and the body, and pressurised fluid is supplied to it through openings 6. A flange 8 with a groove 7 is

provided at the nozzle edge. These serve to seal the inlet opening 9. Plates 3 form a conical channel with a polygonal opening. The equivalent diameter of the channel at its minimum cross-section is 0.3–0.5 mm.

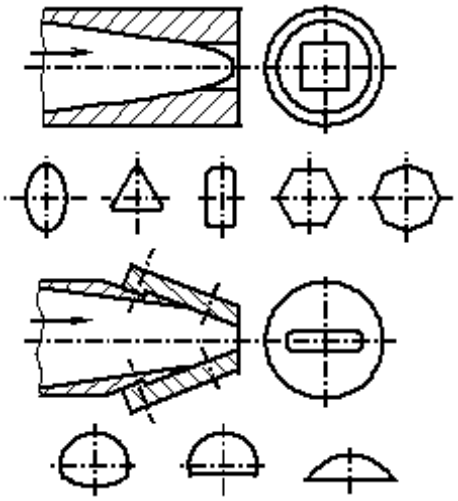


Fig. 22. Schemes of nozzle devices with non-circular openings.

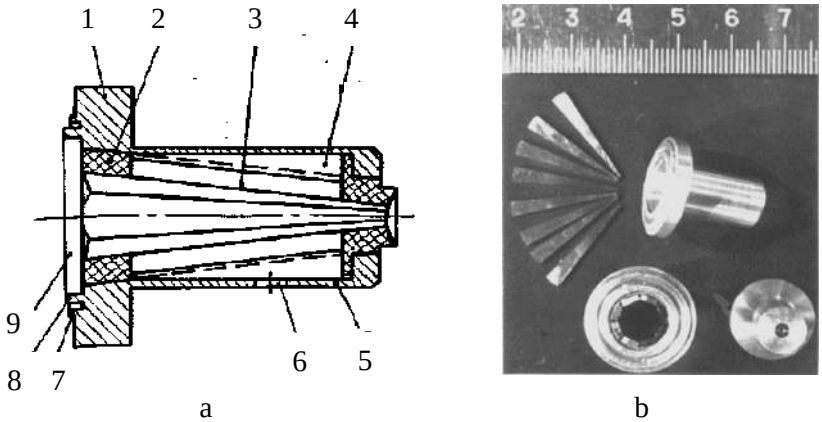


Fig. 23. Assembled nozzle made of wedge-shaped plates: (a) design scheme; (b) nozzle parts and external appearance; 1 – body; 2 – polymer for sealing the plates; 3 – wedge-shaped plates; 4 – cavity between the plates and the body; 6 – fluid supply openings; 7 – sealing groove; 8 – flange; 9 – inlet opening.

The plates (Fig. 23b) are made of 95Х18-Ш steel and heat-treated to a hardness of 62–64 HRC. The finishing operation involves grinding the working surface of the plate, with the grooves and ridges oriented along its length. Subsequently, the plates belonging to a particular nozzle or receiver channel are ground together in a stack to form a special microprofile on their side surfaces. The grooves of this side-surface microprofile are oriented perpendicular to the longitudinal axis of the plate. Micromilling methods were used in machining the plates [25, 29].

The microprofile of the working surfaces of the plates forming the nozzle flow passage has a system of longitudinal grooves. Therefore, as fluid flows at high velocity through the nozzle channel, boundary layers develop along the grooves and ridges of the microprofile. This flow is resistant to separation and transition to turbulence, which reduces energy losses in the nozzles. The anisotropy of this microprofile considerably increases nozzle wear resistance. Solid contaminant particles carried by the fluid at high velocity interact with the local ridges between the grooves. This causes local wear of the ridges and consequently improves the quality of the internal nozzle surface.

The slots between the plates are used to inject fluid into or withdraw it from the boundary layers on the nozzle surface. The fluid passes through the slots between the side surfaces of the plates. Fluid injection or suction substantially reduces flow separation in the nozzle channel.

An assembled nozzle with a rectangular opening cross-section was developed, consisting of two body parts with inserts (Fig. 24a).

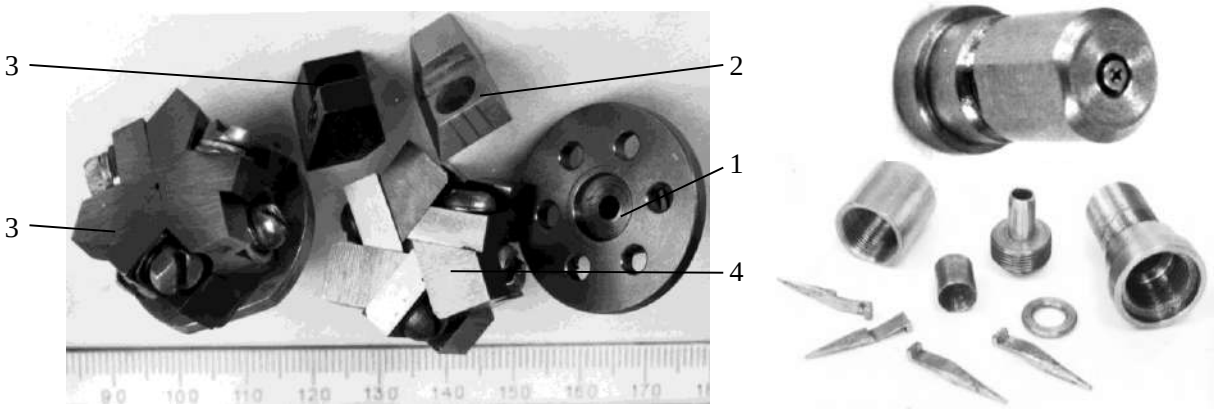


a b

Fig. 24. External appearance and parts of assembled nozzle devices: (a) adjustable nozzle device with a rectangular outlet opening; (b) nozzle device with a curved channel.

The nozzle size is adjusted by moving the inserts. A nozzle with a curved channel was manufactured in a similar way (Fig. 24b). The dimensions of the rectangular nozzle opening are (0.2–0.5) × 0.5 mm.

Nozzles with adjustable hexagonal opening dimensions are assembled on flange 1 from separate prismatic parts 2, 3, and 4 with high surface hardness (Fig. 25a).



a b

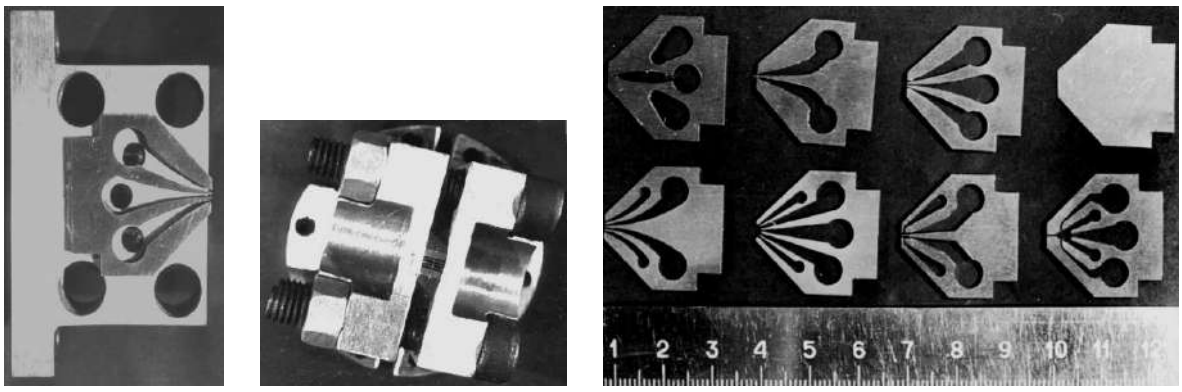
Fig. 25. Assembled nozzle devices and their parts: (a) nozzle device with a hexagonal opening cross-section; (b) nozzle with a cross-shaped opening and a collet mechanism for adjusting its dimensions; 1 – flange; 2, 3, 4 – prismatic parts.

A nozzle with a small cross-shaped opening has a collet mechanism for adjusting the opening dimensions (Fig. 25b). Manufacturing the receiver channels presents a complex technological problem.

Jet devices with rectangular receiver channel openings are constructed using a set of plates with shaped slots. The plates are placed between the flat surfaces of the body parts and sealed to form a stack (Fig. 26a, b).

The plate thickness is 0.08–0.2 mm, and the minimum slot width is 0.1–0.3 mm (Fig. 26c). Assembled receiver channels with non-circular openings were proposed and tested experimentally.

A nozzle device with two converging–diverging receiver channels separated by a spacer allows channels with segment-shaped openings to be formed (Fig. 27).



a b c

Fig. 26. Design of a jet device with receiver channels formed by a stack of plates: (a) placement of a plate on a body part; (b) assembled device with eight channels with rectangular openings; (c) plates with shaped slots.

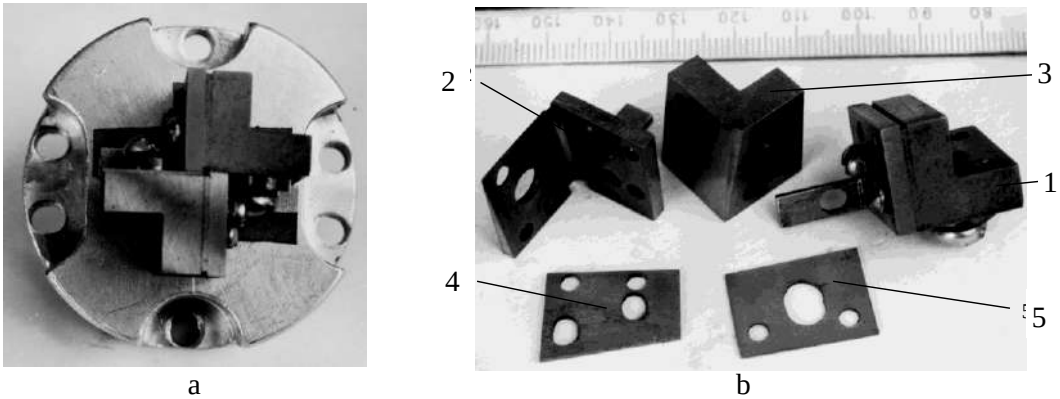


a b

Fig. 27. External appearance and parts of receiver channel blocks with segment-shaped openings.

The proposed designs allow adjustable receiver channels with opening dimensions of 0.1–0.5 mm to be manufactured from high-carbon chromium and chromium–molybdenum steels. Appropriate heat treatment provides a surface hardness of 62–65 HRC in the channel flow passages. This improves the operational reliability and service life of high-pressure jet devices.

The proposed assembled design of the receiver channels (Fig. 28) allows adjustment of the dimensions of their rectangular outlet openings.



a b

Fig. 28. Receiver channel block with rectangular openings: (a) general view of the block; (b) block parts; 1, 3 – body parts; 2 – insert; 4, 5 – flat plates for adjusting the opening dimensions.

The opening dimensions are adjusted by moving flat plates 4 and 5, with thicknesses of 0.2 and 0.5 mm, installed between body parts 1, 3 and insert 2. This device allows adjustment

of the rectangular opening dimensions within the ranges (0.2–0.5) × 0.5 mm and (0.1–1.0) × 0.2 mm.

Discussion.

The use of industrial water as the working medium in hydraulic control systems for wheelless ground robotic complexes is a matter for discussion. The difficult operating conditions are undoubtedly an argument in favour of industrial water. On the other hand, the dimensions of wheelless robotic complexes and the specified loads require the use of high-pressure systems operating at 50–60 MPa. Such systems generally operate with mineral oil. The use of water is problematic. This problem is addressed by using high-pressure jet devices.

To improve efficiency, the cross-sectional areas of the channel and nozzle openings are minimised. The minimum cross-section is limited by the possibility of channel blockage. To prevent blockage, unsteady fluid flow incorporating periodic isolated three-dimensional vortices is proposed for the nozzle channels. These vortices are formed by pulsed fluid flows generated by resonant pulsation systems.

Another matter for discussion is the change in the energy balance of a jet device when vortex systems are introduced into its flow passage. Energy is expended on forming isolated vortices. Overall, the energy expenditure of the device increases. However, since the fraction of energy used to form vortices is small, only a slight reduction in the efficiency of the hydraulic control device should be expected. Most jet devices are flow-through devices. All the energy of the fluid flowing through the nozzle is lost. Therefore, introducing vortex systems does not change the overall energy balance of the device.

In most cases, vortex systems increase the mean equivalent hydraulic resistance of the device. This corresponds to a reduction in the fluid flow rate through the nozzle at constant pressure. The reduced flow rate decreases the power losses of the flow-through device. Therefore, the presence of vortex systems in the flow passage of a jet device will reduce the energy consumed by the hydraulic control jet device. This reduction depends on the design parameters and can be optimised.

Another matter for discussion is the usefulness of analysing singular flow regions in jet and vortex devices. The complexity of the hydrodynamic processes provides an argument in favour of such analysis.

Both laminarised and fully developed turbulent fluid flows occur in jet devices. However, the flow regimes are generally transitional. Laminar flow loses stability, and partial transition to turbulence occurs. Singular regions are present in all flow regimes. They are closely related to the flow boundary conditions and, accordingly, to the specific geometry of the jet devices. Singular regions characterise fundamental processes in fluid mechanics: blockage and cavitation. Therefore, analysing singular flow regions is useful and provides effective means of studying the features of the working processes and characteristics of jet devices.

Conclusions.

1. Analysis of the specific operating conditions and the proposed design solutions for hydraulic control systems of wheelless ground robotic complexes showed that the use of conventional hydraulic control devices would significantly reduce the operational reliability and functionality of these systems. The main reason is the high contamination level and aggressiveness of the working medium, namely industrial water at pressures above 25 MPa.

2. To improve the operational reliability of wheelless robots, it is proposed to use specially developed high-pressure jet and vortex devices (20–30 MPa) as components of hydraulic control systems. These devices allow a working fluid filtration rating of 25–50 μm.

3. The components were developed on the basis of studies of the working processes in jet and vortex devices. Numerical studies of fluid flow parameters using the finite element and finite difference methods were confirmed and refined by experimental studies of laminar and turbulent high-pressure fluid jets. Fluid flow patterns were established in singular regions

where the stress and rate-of-strain tensors become degenerate. The effect of three-dimensional high-pressure fluid flows of finite width on the surface wear of jet device parts was determined.

4. It was demonstrated that the proposed innovative high-pressure vortex devices enable the development of highly reliable hydraulic control devices with low sensitivity to working fluid contamination. Vortex devices allow the minimum flow passage dimensions of first-stage hydraulic amplifiers to be increased from 0.3 mm to 0.5 mm without reducing their energy efficiency. This relaxes the working fluid filtration requirements from the 5–10 μm required by conventional hydraulic control devices to 25–50 μm, which is typical of industrial water used as the working medium in hydraulic systems.

5. The features of the static characteristics of high-pressure jet devices were established through studies of their working processes. In particular, stable operating ranges were substantiated for flow rates up to 40% and pressures up to 80% of their maximum values, with linear ranges of the control characteristics reaching 60%. It was demonstrated that these devices operate reliably for 10 million cycles.

6. The features of the dynamic characteristics of jet devices were determined, particularly the presence of continuous random high-frequency pressure fluctuations in the range of 500–1000 Hz. Analysis of the correlation and spectral properties of these fluctuations provided the basis for developing high-pass filters to ensure stable characteristics and eliminate resonant operating conditions in jet devices. The use of pulsating parameter variations was proposed to reduce device sensitivity to working fluid contamination. This enabled reliable device operation with a working fluid filtration rating of 25–50 μm.

7. Promising manufacturing approaches were substantiated for the components of hydraulic control systems for wheelless ground robotic complexes, including high-pressure jet and vortex devices. The development of assembled nozzles and receiver channels is recommended. This allows device parts to be manufactured from corrosion-resistant and wear-resistant chromium and chromium–molybdenum steels, with finish grinding of the internal surfaces of small nozzles and channels. Micromilling methods were proposed for forming an anisotropic microprofile on these internal surfaces. This provides the required anisotropy of the microprofile of the machined internal nozzle and channel surfaces at a hardness of 62–64 HRC and, accordingly, considerably increases device wear resistance.

References

1. Isakova T.O. Problemy formuvannia stratehichnykh priorytetiv derzhavnoi polityky shchodo rozvytku robototekhniky: perspektyvy dlia Ukrainy. Ofitsiinyi sait Natsionalnoho Instytutu stratehichnykh doslidzhen vid 13.09.2019 r. [Elektronnyi resurs]. Rezhym dostupu: https://niss.gov.ua/doslidzhennya/informaciyni-strategii/problemi-formuvannya-strategichnikh-prioritetiv-derzhavnoi.

2. Strutynskyi, V. B., Hurzhii A. M. Nazemni robotyzovani kompleksy: monohrafiia. Zhytomyr: PP «Ruta», 2023. 497 s. https://ela.kpi.ua/handle/123456789/57111

3. Chepkov I. B., Dovhopolyi A. S., Husliakov O. M. Kontseptualni zasady stvorennia vitchyznianykh udarno-rozviduvalnykh nazemnykh robotyzovanykh kompleksiv vazhkoho klasu. Ozbroiennia ta viiskova tekhnika. Kyiv: TsNDI OVT, 2019. 3 (23). 16–25.

4. Strutynsky, V., Hurzhii, A., Kozlov L. Determination of static equilibrium conditions of a mobile terrestrial robotic complex. *Natsional'nyi Hirnychyi Universytet. Naukovyi Visnyk*, 2019. 5. 79-86. https://doi.org/10.29202/nvngu/2019-5/7

5. Strutynsky, V., Kotsiuruba, V., Dovhopoliy, A., Husliakov, O., Budianu, R., Kolos, O., Hrechka, I. Substantiating the requirements to functional indicators for the manipulators of mobile robotic demining complexes. *Eastern-European Journal of Enterprise Technologies*, 2019. 5(7 (101). 42–50. https://doi.org/10.15587/1729-4061.2019.178466

6. Shuhurov O. S. Rozvytok viiskovykh nazemnykh robotyzovanykh system v konteksti novykh kontseptsii upravlinnia: perspektyvy Ukrainy. http://sp.niss.gov.ua/content/ articles/files/27-1445867323.pdf.

7. Moosavi S. K. R., Zafar M. H., Sanfilippo F. Snake robots: A state-of-the-art review on design, locomotion, control, and real-world applications. *Mechatronics*, 2025. 112. 103418. https://doi.org/10.1016/j.mechatronics.2025.103418

8. Bianchi G., Lanzetti L., Mariana D., Cinquemani S. Bioinspired Design and Experimental Validation of an Aquatic Snake Robot. *Biomimetics*, 2024. 9. 87. https://doi.org/10.3390/biomimetics9020087

9. Bi Zh., Zhou Q., Fang H. A worm-snake-inspired metameric robot for multi-modal locomotion: Design, modeling, and unified gait control. *International Journal of Mechanical Sciences*, 2023. 254. 108436. https://doi.org/10.1016/j.ijmecsci.2023.108436

10.Panchenko A.I., Voloshyna A.A., Panchenko I.A., Voloshyn A.A. Proektuvannia mekhatronnykh system z zadanymy vykhidnymy kharakterystykamy. *Pratsi TDATU*. Melitopol: TDATU. 2020. 20 (4). 18–35. https://doi.org/10.31388/2078-0877-2020-20-4-18-35

11. Panchenko A.I., Voloshyna A.A., Panchenko I.A., Voloshyn A.A. Model hidravlichnoho pryvodu mekhatronnoi systemy. *Pratsi TDATU*, 2018. 18 (2). 59–83. https://doi.org/10.31388/2078-0877-18-2-58-82

12. Panchenko A., Voloshina A., Kiurchev S. et al. Development of the universal model of mechatronic system with a hydraulic drive. *Eastern-European Journal of Enterprise Technologies: Applied mechanics*, 2018. 4(7 (94)). 51–60. https://doi.org/10.15587/1729-4061.2018.139577

13. Panchenko A.I., Voloshyna A.A., Rozhniatovskyi V.V., Zasiadko A. I. Model hidravlichnoho pryvodu mekhatronnoi systemy z planetarnym hidromotorom. *Promyslova hidravlika i pnevmatyka*, 2024. 2 (74). 12–32. https://doi.org/10.32782/1994-4691-2024-2-74-2

14.Panchenko A.I., Voloshyna A.A., Panchenko I.A., Voloshyn A.A. Doslidzhennia dynamichnykh kharakterystyk mekhatronnykh system z hidravlichnym pryvodom. *Pratsi TDATU*, 2020. 20 (4). 58–72. https://doi.org/10.31388/2078-0877-2020-20-4-58-72

15. Panchenko A.I., Voloshyna A.A., Panchenko I.A., Voloshyn A.A. Zmina funktsionalnykh parametriv mekhatronnykh system z planetarnymy hidromotoramy pry riznykh umovakh ekspluatatsii. *Naukovyi visnyk TDATU*, 2025. 15 (2). 127–135. https://doi.org/10.32782/2220-8674-2025-15-2-15

16. Strutynskyi V.B., Kolot O.V. Matematychne modeliuvannia stokhastychnykh protsesiv u systemakh pryvodiv. Kramatorsk: ZAT "Tyrazh-51", 2005. 530 c.

17. Li R., Wei W., Liu H., Geng X., Cui J., et al. Design and experimental validation of a valve-distributed pump. *Proceedings of the Institution of Mechanical Engineers, Part C: Journal of Mechanical Engineering Science*, 2024. 238 (12). 5488–5497. https://doi.org/10.1177/09544062231220736

18. Xu, S., He, Y., Chen, Y., Nan, M., & Luo, M. Design, modelling and control of hyper-redundant robots in constrained environments: A review. *Robotics and Autonomous Systems*, 2026. 204. 105572. https://doi.org/10.1016/j.robot.2026.105572

19. Andersson, C. A. The unmanned ground vehicles to be used in future military operations. *Tiede Ja Ase*, 2022. 2021(79). https://journal.fi/ta/article/view/113769

20. Strutynskyi V.B. Matematychne modeliuvannia protsesiv ta system mekhaniky. Zhytomyr: ZhITI, 2001. 611 s.

21. Sun E., Camacho-Arreguin J., Zhou J., et al. Macro-mini collaborative manipulator system for welding in confined environments. *Robotics and Computer-Integrated Manufacturing*, 2025. 94. 102975. https://doi.org/10.1016/j.rcim.2025.102975

22. Anguek O., Belkacem B. Multi-objective design optimization of a Turret's U-bracket mounted on moving platform. *Proceedings of the Institution of Mechanical Engineers Part C Journal of Mechanical Engineering Science*, 2022. 236 (24). (2), 11371–11388. https://doi.org/10.1177/09544062221115106

23. Le Q. D., Yang E. Adaptive Fault-Tolerant Tracking Control for Multi-Joint Robot Manipulators via Neural Network-Based Synchronization. *Sensors*, 2024. 24 (21). 6837. https://doi.org/10.3390/s24216837

24. Jia, B. Vibration Propagation Characteristics of Micro-Milling Tools. *Machines*, 2022. 10. 946. https://doi.org/10.3390/machines10100946

25. Bai Q, Wang P, Cheng K, et al. Machining dynamics and chatters in micro-milling: A critical review on the state-of-the-art and future perspectives. *Chinese Journal of Aeronautics*, 2024. 37(7). 59–80. https://doi.org/10.1016/j.cja.2024.02.022

26. Mobilnyi robototekhnichnyi kompleks z dystantsiinym keruvanniam: pat. 127035 Ukraina : B25J 5/00, B25J 9/00, B25J 5/02 (2006.01), B25J 9/06 (2006.01), B25J 19/00, B25J 19/04 (2006.01) /

V.B. Strutynskyi; A.M. Hurzhii; S.Yu. Vakulenko; V.V. Novak. – № a201908587; zaiavl. 18.07.2019; opubl. 22.03.2023, Biul. № 12/2023. https://sis.nipo.gov.ua/uk/search/detail/1727728/

27. Bezkolisnyi robot zaiavka pa patent Ukrainy: B62D 57/04(2026.01) / V.B. Strutynskyi. – № a214407165; zaiavl. 18.08.2026.

28. Strutynskyi V.B. Tenzorni matematychni modeli protsesiv ta system: monohrafiia. Zhytomyr : ZhDTU, 2005. 635 s.

29. Strutynskyi V. B., Perfilov I. V. Vibratsiini protsesy mekhanichnoi obrobky: monohrafiia. Kyiv: Khimdzhest, 2015. 579 s.

Дата першого надходження статті до видання 05.09.2026
Дата прийняття статті до друку після рецензування 09.10.2026
Дата публікації (оприлюднення) статті 04.11.2026
Стаття поширюється на умовах ліцензії відкритого доступу(CC BY 4.0)

ЕЛЕМЕНТНА БАЗА СИСТЕМ ГІДРОАВТОМАТИКИ БЕЗКОЛІСНИХ НАЗЕМНИХ РОБОТИЗОВАНИХ КОМПЛЕКСІВ

В. Б. Струтинський[1]
[1] *Національний технічний університет України «КПІ імені Ігоря Сікорського»,*

Анотація

Стаття присвячена розробленню елементної бази систем гідроавтоматики безколісних наземних роботизованих комплексів високої прохідності. Розглянуті типові безколісні наземні роботизовані комплекси які мають центральну частину яка ковзає по поверхні за допомогою інерційних рушіїв і оснащена гнучкими протяжними (довжиною 2..3 м) периферійними елементами на кінцях яких встановлені ножі, пили або фрези для руйнування перешкод. Комплекс має великогабаритний (порядку 4 м) маніпулятор, що забезпечує огляд і дослідження поверхні , орієнтацію та зв'язок. Безколісні наземні роботизовані комплекси включають спеціальні агрегати та системи гідроприводу та гідроавтоматики з робочим середовищем типу технічної води. Їх запропоновано реалізувати з використанням інноваційної елементної бази на основі струменевих та вихрових пристроїв і агрегатів високого тиску (порядку 25 МПа). Наведені розроблені схемні рішення інноваційних струменевих та вихрових пристроїв. Теоретично та експериментально досліджені гідродинамічні процеси в пристроях. Встановлено, що сингулярні області течії, де вироджується тензор швидкостей деформацій, визначають робочі процеси струменевих та вихрових пристроїв. Наведено результати досліджень статичних та динамічних характеристик струменевих пристроїв які складають елементну базу. Запропонована конструктивна реалізація та технологічні методи виконання малорозмірних (порядку 0.3 мм) каналів підвищеної зносостійкості. Технологічні методи апробовані розробленими і виготовленими експериментальними зразками.

Ключові слова: струменеві агрегати, вихрові пристрої, сингулярні області, турбулентні струмені, статичні характеристики.